REPORT DOCUMENTATION PAGE

Form Approved OMB NO. 0704-0188

1. REPORT DATE (DD-MM-YYYY)	2. REPORT TYPE	3. DATES COVERED (From - To)
07-09-2013	Final Report	1-Jul-2007 - 31-Mar-2013

4. TITLE AND SUBTITLE

Miniaturization and Optimization of Nanoscale Resonant Oscillators

5a. CONTRACT NUMBER
W911NF-07-1-0338

5b. GRANT NUMBER

5c. PROGRAM ELEMENT NUMBER
7D10AI

6. AUTHORS

PI-Y. Fainman, co-PIs C. Tu, V. Lomakin, B. Slutsky and M. Nezhad

5d. PROJECT NUMBER

5e. TASK NUMBER

5f. WORK UNIT NUMBER

7. PERFORMING ORGANIZATION NAMES AND ADDRESSES

University of California - San Diego
9500 Gilman Drive
M/C 0934
La Jolla, CA 92093 -0934

8. PERFORMING ORGANIZATION REPORT NUMBER

9. SPONSORING/MONITORING AGENCY NAME(S) AND ADDRESS(ES)

U.S. Army Research Office
P.O. Box 12211
Research Triangle Park, NC 27709-2211

10. SPONSOR/MONITOR'S ACRONYM(S)
ARO

11. SPONSOR/MONITOR'S REPORT NUMBER(S)
53045-EL-DRP.7

12. DISTRIBUTION AVAILIBILITY STATEMENT

Approved for Public Release; Distribution Unlimited

13. SUPPLEMENTARY NOTES

The views, opinions and/or findings contained in this report are those of the author(s) and should not contrued as an official Department of the Army position, policy or decision, unless so designated by other documentation.

14. ABSTRACT

Current microscale semiconductor laser resonators may attain small modal volumes but require structures that are large compared to the wavelength, such as photonic crystals [11] or Bragg mirrors [12]. Metallic coatings provide stronger confinement of light and consequently higher device-packing density and therefore have been proposed for reducing the size of semiconductor nanowire lasers [13, 14]. The drawback of using metals, however, is their high dissipation losses at optical frequencies. Lasing in three-dimensional (3D) subwavelength metal-coated cavities

15. SUBJECT TERMS

Nanolasers

16. SECURITY CLASSIFICATION OF:			17. LIMITATION OF ABSTRACT	15. NUMBER OF PAGES	19a. NAME OF RESPONSIBLE PERSON
a. REPORT	b. ABSTRACT	c. THIS PAGE			Yeshaiahu Fainman
UU	UU	UU	UU		19b. TELEPHONE NUMBER 858-534-8909

Report Title

Miniaturization and Optimization of Nanoscale Resonant Oscillators

ABSTRACT

Current microscale semiconductor laser resonators may attain small modal volumes but require structures that are large compared to the wavelength, such as photonic crystals [11] or Bragg mirrors [12]. Metallic coatings provide stronger confinement of light and consequently higher device-packing density and therefore have been proposed for reducing the size of semiconductor nanowire lasers [13, 14]. The drawback of using metals, however, is their high dissipation losses at optical frequencies. Lasing in three-dimensional (3D) subwavelength metal-coated cavities operating at cryogenic temperatures to reduce the dissipation losses in the metal and increase the gain in the semiconductor has been reported [8]. We show that the losses in metal coated gain waveguides, as well as 3D laser resonators, can be significantly reduced by introducing a low index "shield" layer between the gain medium and the metal.

Enter List of papers submitted or published that acknowledge ARO support from the start of the project to the date of this printing. List the papers, including journal references, in the following categories:

(a) Papers published in peer-reviewed journals (N/A for none)

Received		Paper
08/29/2011	1.00	Qian Ding, Amit Mizrahi, Yeshaiahu Fainman, Vitaliy Lomakin. Dielectric shielded nanoscale patch laser resonators, Optics Letters, (05 2011): 0. doi: 10.1364/OL.36.001812
08/29/2011	4.00	Amit Mizrahi, Yeshaiahu Fainman. Negative radiation pressure on gain medium structures, Optics Letters, (10 2010): 0. doi: 10.1364/OL.35.003405
08/29/2011	5.00	D. Van Orden, Y. Fainman, V. Lomakin. Twisted chains of resonant particles: optical polarization control, waveguidance, and radiation, Optics Letters, (07 2010): 0. doi: 10.1364/OL.35.002579
08/29/2011	6.00	O. Bondarenko, A. Simic, Q. Gu, J.H. Lee, B. Slutsky,M. P. Nezhad and Y. Fainman. Wafer Bonded Subwavelength Metallo-Dielectric Laser, IEEE Photonics Journal, (06 2011): 608. doi:
TOTAL:		**4**

Number of Papers published in peer-reviewed journals:

(b) Papers published in non-peer-reviewed journals (N/A for none)

Received		Paper
TOTAL:		

Number of Papers published in non peer-reviewed journals:

(c) Presentations

Number of Presentations: 0.00

Non Peer-Reviewed Conference Proceeding publications (other than abstracts):

Received	Paper

TOTAL:

Number of Non Peer-Reviewed Conference Proceeding publications (other than abstracts):

Peer-Reviewed Conference Proceeding publications (other than abstracts):

Received	Paper	
08/29/2011	3.00	Y. Fainman, D. Tan, S. Zamek, O. Bondarenko, A. Simic, A. Mizrahi, L. Feng, M. Nezhad, B. Slutsky. Active and passive nanophotonics for information systems applications, 2011 IEEE Winter Topicals (WTM). 2011/01/09 03:00:00, Keystone, CO, USA. : ,
08/29/2011	2.00	Aleksandar Simic, Olesya Bondarenko, Qing Gu, Jin Lee, Mercedeh Khajavikhan, Boris Slutsky, Maziar P. Nezhad, Yeshaiahu Fainman. Fabrication approaches for metallo-dielectric nanolasers, 2011 IEEE Winter Topicals (WTM). 2011/01/09 03:00:00, Keystone, CO, USA. : ,

TOTAL: **2**

Number of Peer-Reviewed Conference Proceeding publications (other than abstracts):

(d) Manuscripts

Received	Paper

TOTAL:

Number of Manuscripts:

Books

Received Paper

TOTAL:

Patents Submitted

Patents Awarded

Awards

Graduate Students

NAME	PERCENT_SUPPORTED	Discipline
Chang, Ruinan	0.50	
Freeman, Lindsay Michelle	0.50	
Kuang, Yanjin	0.25	
Liu, Christopher Michael	0.50	
Smalley, Joseph Stephen Th	0.50	
Wingad, Brett David	0.50	
FTE Equivalent:	**2.75**	
Total Number:	**6**	

Names of Post Doctorates

NAME	PERCENT_SUPPORTED
Kats, Michael	1.00
Khajavikhan, Mercedeh	1.00
Li, Hua	1.00
FTE Equivalent:	**3.00**
Total Number:	**3**

Names of Faculty Supported

NAME	PERCENT_SUPPORTED	National Academy Member
Fainman, Yeshaiahu	0.67	
Lomakin, Vitaliy	0.50	
FTE Equivalent:	**1.17**	
Total Number:	**2**	

Names of Under Graduate students supported

NAME	PERCENT SUPPORTED
FTE Equivalent:	
Total Number:	

Student Metrics

This section only applies to graduating undergraduates supported by this agreement in this reporting period

The number of undergraduates funded by this agreement who graduated during this period:	0.00
The number of undergraduates funded by this agreement who graduated during this period with a degree in science, mathematics, engineering, or technology fields:.....	0.00
The number of undergraduates funded by your agreement who graduated during this period and will continue to pursue a graduate or Ph.D. degree in science, mathematics, engineering, or technology fields:.....	0.00
Number of graduating undergraduates who achieved a 3.5 GPA to 4.0 (4.0 max scale):	0.00
Number of graduating undergraduates funded by a DoD funded Center of Excellence grant for Education, Research and Engineering:	0.00
The number of undergraduates funded by your agreement who graduated during this period and intend to work for the Department of Defense	0.00
The number of undergraduates funded by your agreement who graduated during this period and will receive scholarships or fellowships for further studies in science, mathematics, engineering or technology fields:	0.00

Names of Personnel receiving masters degrees

NAME
Total Number:

Names of personnel receiving PHDs

NAME
Total Number:

Names of other research staff

NAME	PERCENT SUPPORTED
Pang, Lin	0.25
Slutsky, Boris A.	1.00
FTE Equivalent:	**1.25**
Total Number:	**2**

Sub Contractors (DD882)

Inventions (DD882)

Scientific Progress

see attachment

Technology Transfer

Miniaturization and Optimization of Nanoscale Resonant Oscillators (MONRO)

PI-Y. Fainman, co-PIs C. Tu, V. Lomakin,B. Slutsky and M. Nezhad

Department of ECE

University of California, San Diego, la Jolla CA 92093

fainman@ece.ucsd.edu

858-395-2289

1. 0 Introduction

Achieving the most compact footprint for photonic components is an important factor in the design of integrated optical devices. Like most other photonic components, the minimum size for a laser is ultimately governed by the free space wavelength, λ_0. For example, as the size of a conventional Fabry-Perot semiconductor laser is scaled down in all three dimensions towards λ_0, three effects adversely influence the lasing process. First, the roundtrip path of the optical wave in the gain medium is shortened. Second, radiative losses from the end mirrors are increased. Third, the lateral field confinement in the resonator waveguide is reduced, resulting in less overlap of the optical mode with the gain medium. All these effects serve to increase the lasing threshold, and lasing cannot therefore be achieved below a certain size limit. By allowing the laser size to increase in one or two dimensions, it is possible to reduce the physical size of the laser in the remaining dimension(s) to values below this limit. For example, the disk thickness in whispering-gallery-mode (WGM) lasers [1] can be reduced to a fraction of the free-space wavelength [2], but to compensate for this thickness reduction the disk diameter should be increased accordingly. The ultimate challenge in this respect is concurrent reduction of the resonator size in all three dimensions, while still satisfying the requirements for lasing action.

The size of an optical cavity can be defined using different metrics (for example, the physical dimensions of the cavity or the size of the optical mode). However, if the goal of size reduction is to increase the integration density (for example, in a laser array), the effective cavity size should account for both the overall physical dimensions of the resonator and the spread of the optical mode beyond the physical boundary of the resonator. By this token, most conventional dielectric laser cavities are not amenable to dense integration because they either have a large physical footprint or a large effective mode. For example, distributed Bragg resonators [3] and photonic-crystal cavities [4] (both of which can be designed to have very

small mode volumes) have physical footprints that are many wavelengths in size, due to the several Bragg layers or lattice periods that are required for maintaining high finesse. On the other hand, it has been demonstrated that the diameter of thick (λ_0/n) microdisk lasers can be reduced below their free-space emission wavelength [5]; however, the spatial spread of the resultant modes (which have low azimuthal numbers owing to the small disk diameters) into the surrounding space beyond the physical boundaries of the disks may lead to mode coupling and formation of 'photonic molecules' in closely spaced disks [6]. To illustrate the case, the M=4 WGM for a semiconductor disk with radius r_c=460 nm and height h_c=480 nm (Fig. 1a) is shown in Fig. 1b, clearly indicating the radiative nature of the mode and its spatial spread, which, as mentioned, can lead to mode coupling with nearby structures.

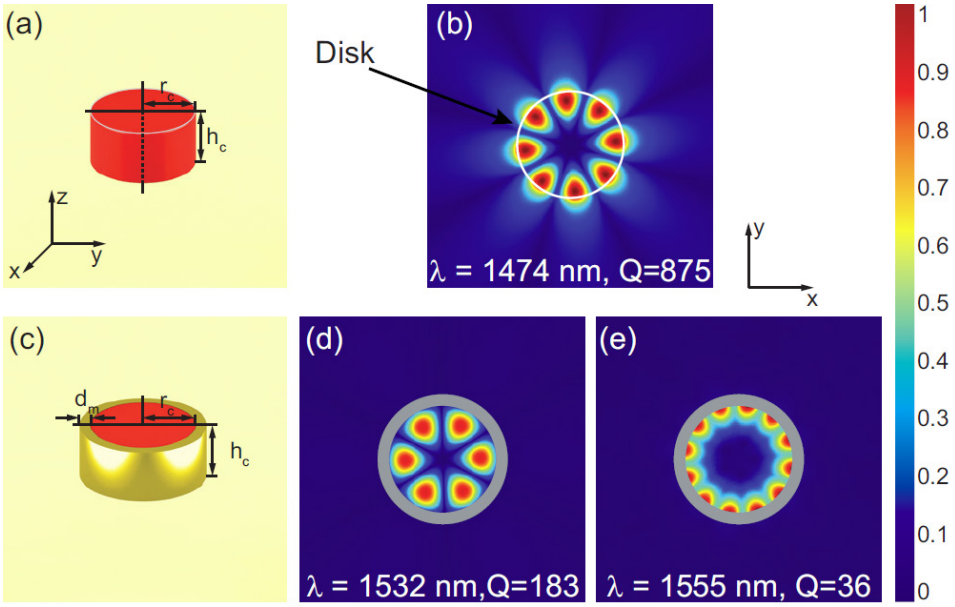

Figure1. The *M*=4 whispering gallery resonance for a thick semiconductor disk (a) is shown in (b). (r_c=460nm, h_c=480nm, n_{semi}=3.4). Note the spatial spread of the mode compared to the actual disk size. (c) The same disk encased in an optically thick (d_m=100nm) gold shield will have well-confined reflective (d) and plasmonic (e) modes but with much higher mode losses. $|\boldsymbol{E}|$is shown in all cases and the section plane is horizontal and through the middle of the cylinder.

One approach for alleviating these issues is to incorporate metals into the structure of dielectric cavities, because metals can suppress leaky optical modes and effectively isolate them from their neighboring environment. The modes in these metallo-dielectric cavities can be grouped into two main categories: (i) surface bound (that is, surface plasmon polariton (SPP)) resonant modes and (ii) conventional resonant modes, resulting purely from reflections within the metal cavity. Although they are highly confined, the disadvantage of plasmonic modes is

their high loss, which is caused by the relatively large mode overlap of the optical field with the metal (compared to the reflective case). Owing to the high Joule loss at telecommunication and visible wavelengths, the lasing gain threshold for such cavities can be very large. On the other hand, the negative permittivity of metals not only allows them to support SPP modes, but also enables them to act as efficient mirrors. This leads to the second class of metallo-dielectric cavity modes, which can be viewed as lossy approximations of the modes in a perfectly conducting metal cavity. Because the mode volume overlap with the metal is usually smaller than in the plasmonic case, in this type of cavity it is possible to achieve higher Q factors and lower lasing gain thresholds, albeit at the expense of reduced mode confinement (compared to plasmonic modes). In general, both types of mode can exist in a real metal cavity. Embedding the aforementioned gain disk in a gold shield (Fig. 1c) effectively confines the resonant modes while increasing Joule losses. As discussed, the surfacebound plasmonic mode (Fig. 1e) has both a higher M number and higher losses (M= 6, Q=36) compared to the non-plasmonic mode (Fig. 1d, M=3, Q =183). It should be noted that even though the metal shield is the source of Joule loss, the large refractive index of the semiconductor core ($n_{semi} \approx 3.4$) aggravates the problem and increases both the plasmonic and Fresnel reflection losses. For SPP propagation on a (planar) semiconductor–metal interface, the threshold gain for lossless propagation is proportional to n^3_{semi}. This means that, even though high-Q plasmonic modes can exist inside metal cavities with low-index cores (for example, silica, n =1.48), using this approach to create a purely plasmonic, room-temperature semiconductor laser at telecommunication wavelengths will be very challenging, due to the order-of-magnitude increase in gain threshold. However, plasmonic modes have also an advantage in co-localising the emitters with the resonant mode volume, thereby, leading to a more efficient emission into the lasing mode. This mode of opearation will also be further discussed below, but at this point we will focus on novel photonic mode resonators.

One possible solution for overcoming the metal loss obstacle is to reduce the temperature of operation. This will have two coinciding benefits, a reduction of the Joule losses in the metal and an increase in the amount of achievable semiconductor gain. Recently Hill and colleagues [8] have demonstrated cryogenic lasing from gold-coated semiconductor cores with diameters as small as 210 nm. However, in this case the metal is directly deposited on the semiconductor core (with a 10-nm SiN insulation layer between). As a result, owing to the large overlap of the mode

with the metal, the estimated room-temperature cavity Q is quite low. The best case is ~180 for a silver coating (assuming the best reported value for the permittivity of silver [9]). This corresponds to an overall gain threshold of ~1,700 cm^{-1} and is quite challenging to achieve at room temperature. Even though this device lases when cooled to cryogenic temperatures, it would be challenging to achieve room-temperature lasing with the same approach and a similarly sized cavity, due to the constraints imposed by the amount of available semiconductor gain and metal losses. The gain coefficient reported for optically pumped bulk InGaAsP emitting at 1.55 mm is reported to be ~200 cm^{-1}. Electrically pumped multiple quantum wells (MQWs), on the other hand, have been reported to have higher material gain coefficients of over 1,000 cm^{-1}. Also, recent results obtained from Fabry–Perot-type metallic nanolasers at room temperature indicate that this level of gain is also achievable from bulk InGaAs [10]. However, even if the required gain is achievable at room temperature, efficient operation of the device would still be a challenge due to thermal heating and non-radiative recombination processes (for example, Auger recombination). In particular, to operate a densely packed array of such devices, thermal management would be a major concern, given the requisite intense pumping levels. Consequently, it is extremely important to optimize the resonator design such that the gain threshold is minimized. In the next section we will introduce a novel three-dimensional resonator design that supports photonic modes and allows optimization of resonator geometry and constituent materials for operation with gain threshold that can be achieved in practice.

2.0 Metallo-dielectric resonators

Current microscale semiconductor laser resonators may attain small modal volumes but require structures that are large compared to the wavelength, such as photonic crystals [11] or Bragg mirrors [12]. Metallic coatings provide stronger confinement of light and consequently higher device-packing density and therefore have been proposed for reducing the size of semiconductor nanowire lasers [13, 14]. The drawback of using metals, however, is their high dissipation losses at optical frequencies. Lasing in three-dimensional (3D) subwavelength metal-coated cavities operating at cryogenic temperatures to reduce the dissipation losses in the metal and increase the gain in the semiconductor has been reported [8]. In this section, we show that the losses in metal coated gain waveguides, as well as 3D laser resonators, can be significantly reduced by introducing a low index “shield” layer between the gain medium and the metal.

Consider a composite gain waveguide (CGW) having a gain medium cylindrical core, a shield layer, and a metallic coating, as shown in Fig. 2a. For a given CGW cross section size, the shield layer thickness is then tuned to maximize the confinement of the electric field in the gain medium and reduce the field penetration into the metal. By that, we increase the ability of the device to compensate for the dissipated power with power generated in the gain medium. A direct measure of that is the threshold gain, i.e., the gain required for lossless propagation [15] in the CGW. The field attenuation in the shield layer resembles that of Bragg fibers [16]. The layer adjacent to the core, in particular, is of high importance [17] and is also used to reduce loss in infrared hollow metallic waveguides [18].

Subsequently, we use the CGW model for the design of subwavelength 3D resonators. To confine the light in the longitudinal direction, the CGW is terminated from both sides by a low index "plug" region covered with metal, which forms the closed cylindrical structure shown in Fig. 2b.

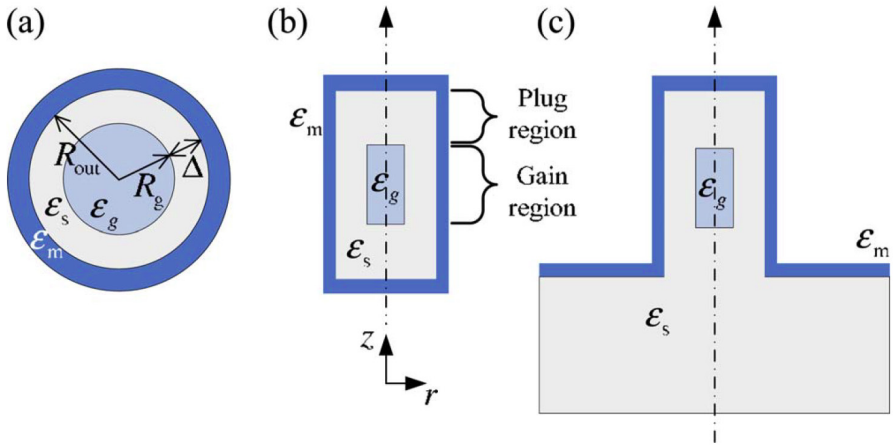

Figure 2. (a) Cross section of the metal-coated composite gain waveguide. (b) Cylindrical closed 3D resonator. (c) Cylindrical open 3D resonator.

A more practical nanolaser configuration from a fabrication point of view is the open structure with a SiO2 substrate shown in Fig. 2c. The inherent radiation losses into the substrate provide means for collecting the laser light, in contrast to the closed structure, where extracting light requires modification of the metal coating, such as making a hole in it. The threshold gain for the 3D resonators, defined as the gain required to compensate for the metal losses in the closed structure or to compensate for both the metal and the radiation losses in the open structure, is shown to be sufficiently low to allow laser action at room temperature.

2.1 Composite gain-dielectric-metal waveguides

Let us first consider the infinite CGW of Fig. 2a, with relative permittivities $\varepsilon_g = \varepsilon_g' + j\varepsilon_g''$, ε_s and $\varepsilon_m = \varepsilon_m' + j\varepsilon_m''$ of the gain medium, the shield layer, and the metal, respectively. Assuming a time dependence of exp $(j\omega t)$, we have $\varepsilon_g'', \varepsilon_m'' > 0$. The radius of the gain medium is R_g, the shield layer thickness is $\Delta = R_{out} - R_g$, and the metallic coating layer begins at radius R_{out}. The eigenmodes of the CGW may be derived from the general solution of the longitudinal fields in each layer having the form

$$U = [AJ_m(k_r r) + BY_m(k_r r)]f(m\varphi)e^{-j\beta z}, \quad (1)$$

where $U = E_z$ or H_z; J_m and Y_m are Bessel functions of the first and second kind, respectively; $k_r = \sqrt{k_0^2\varepsilon - \beta^2}$, $k_0 = \omega/c$; ε is the relative permittivity of the layer; and $f(m\varphi)$ may be expanded by exp $(\pm jm\varphi)$, where the integer m is the azimuthal index. The dispersion relation is found using the transfer matrix method [16]. For the threshold gain ε_g'', the propagation constant β is real, and the threshold gain explicitly satisfies

$$\varepsilon_g'' = \varepsilon_g'' \iint_{Metal} dA\, |\boldsymbol{E}|^2 \Big/ \iint_{Gain} dA\, |\boldsymbol{E}|^2 \quad (2)$$

where the integration in the numerator and denominator is over the cross section of the metal and the each propagation mode may be found by imposing $Im\{\beta\} = 0$ in the dispersion relation and then finding the solutions in the plane of $\left(Re\{\beta\}, \varepsilon_g''\right)$, similarly to [19].

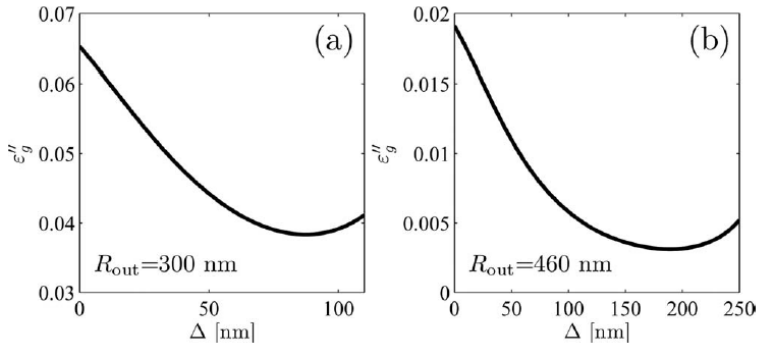

Fig. 3. Threshold gain ε_g'' as a function of the shield thickness Δ for the TE01 mode. (a) R_{out}=300 nm. (b) R_{out}=460 nm.

The effect of the shield layer on the TE01 mode threshold gain is demonstrated in Fig. 3, where ε_g'' is plotted as a function of the shield thickness Δ for a given radius R_{out}=300 nm [Fig.

3a] and R_{out} =460 nm [Fig. 3b]. In the simulations we assume a wavelength of λ=1550 nm, ε_g'=12.5 corresponding to InGaAsP gain medium, ε_s' =2.1 for a SiO_2 shield layer, and $\varepsilon_m' = -95.9 - j11.0$ for a gold coating [20]. The rapid field decay in the gold layer permits us to assume that the metal extends to infinity, whereas in reality a coating layer of 100 nm would suffice. As the shield thickness increases, a lower percentage of the field penetrates into the metal, reducing the losses. On the other hand, the gain material occupies less of the CGW volume, which means that a higher gain is required to compensate for the dissipation losses in the metal. The trade-off between these two processes results in an optimal point in which the threshold gain is minimal. This typical behavior of low-order modes is seen in Fig. 3 for the TE_{01} mode. For R_{out} =300 nm, the improvement of the threshold gain from the Δ=0 (no shield layer) case is by a factor of 1.7, and for R_{out}=460 nm by a factor of 6.1.

For larger radii a lower threshold gain may be achieved, as shown in Fig. 3 and further emphasized in Fig. 4, where the minimal threshold gain ε_g'' is depicted as a function of R_{out} for four low-order modes: TM_{01}, TE_{01}, HE_{11}, and HE_{21}. Having the highest confinement around the gain medium core, the HE_{11} has the lowest threshold gain among the four modes. Generally, for small radii, the shield layer is less effective as it quickly gets the mode below cutoff. For large radii, the threshold gain is low, as the field penetration into the metal is small. The optimal shield layer thickness increases monotonically as a function of R_{out}. For the TE_{01} mode, it ranges between 80 and 330 nm, for R_{out}=250 to 650 nm, respectively.

2.2 Composite gain-dielectric-metal 3D resonators

The role of the metal coating, which is important in the infinite CGW model, becomes even more crucial for creating a 3D resonator. As explained above, the CGW facets are terminated by plug regions, which are short metallic waveguides filled with SiO_2 as seen in Figs. 2b and 2c, in an approach similar to that of Hill *et al.* [8]. The plug ensures strong confinement of the field in the gain region, provided that the mode residing in it is below cutoff, i.e., decaying exponentially in the *z* direction.

For the plug region waveguide, the cutoff is not clearly defined since the modes are significantly different than those of the perfect conducting cylinder waveguide [21]. A reasonable definition for the cutoff is the R_{out} whose β is closest to the origin on the complex β

plane. That cutoff is shown for each one of the modes of Fig. 4 by the vertical lines, providing a qualitative tool for choosing an operation mode for the entire 3D structure, as the chosen radius needs to be to the left of the vertical line corresponding to the operation mode. The smaller the device radius compared to the cutoff radius, the stronger the decay in the plug; consequently, the threshold gain is lower. While the HE_{11} mode achieves the lowest threshold gain for a given *R*out, its cutoff in the plug region is at a small radius; working below this cutoff entails a relatively high threshold gain. It is therefore seen that the TE_{01} mode, which has the highest cutoff of the shown modes, is favorable. The result is having a larger R_{out} but a significantly lower threshold gain. Another advantage of the TE01 is that this mode in the gain region couples only to symmetric TE modes in the plug region, whereas $m>0$ modes are hybrid and may couple to all modes with the same azimuthal index.

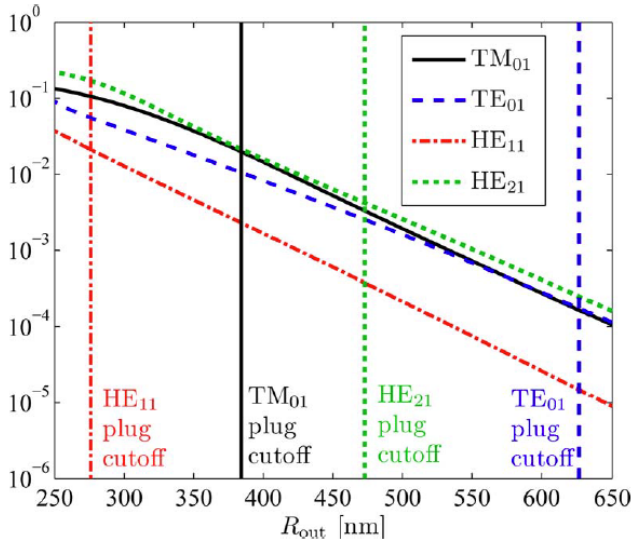

Fig. 4. Minimal threshold gain as a function of R_{out}. The vertical lines show the cutoff of each mode in the 3D resonator plug region.

Using the CGW model at the optimal point of Fig. 3b as a starting point, a 3D closed resonator with R_{out}=460 and 100 nm thick gold coating was designed for the TE_{012} mode. 3D finite element method (FEM) simulation results of the electric field intensity $|\boldsymbol{E}|^2$ normalized to its maximal value are shown in Fig. 5. The overall height of the resonator is 1500 nm, and the overall diameter is 1120 nm, making it smaller than the vacuum wavelength in all three dimensions. The resonance was fine-tuned to a wavelength of 1550 nm by setting the gain cylinder height to be about 480 nm and the shield layer thickness to about 200 nm, which is close to the 190 nm predicted by the CGW model. The threshold gain, however, is in less agreement

with the CGW model; the value for the 3D resonator is $\varepsilon_g'' \cong 0.011$, which corresponds to about 130 cm^{-1}, whereas the CGW model gives about 36 cm^{-1}. This discrepancy is due to the losses occurring in the plug region and the mode deformation at the interfaces between the plug and gain regions, two effects that are not taken into account in the CGW model. Obviously, the longer the resonator, the more accurately the CGW model describes the behavior in the gain region. For instance, a longer resonator with the same radius designed for the TE_{013} mode has a threshold gain of about 95 cm^{-1}.

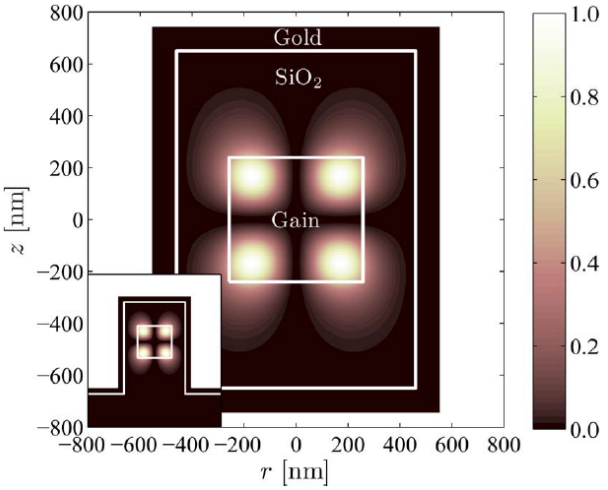

Fig. 5. Cross section of a closed cylindrical 3D subwavelength laser resonator. The electric field intensity $|\boldsymbol{E}|^2$ normalized to its maximal value of the TE_{012} modeis shown. The inset shows a similar open structure.

If the structure shown in Fig. 5 is designed with no shield layer in the gain region, but with the same overall radius and height, then the resulting threshold gain is about 420 cm−1. The gain that may be achieved at room temperature by optical pumping of bulk InGaAsP is about 200 cm^{-1} [22]. It is therefore evident that the shield layer that lowers the threshold gain from 420 to 130 cm−1 is crucial to enable lasing at room temperature. Slightly modifying the structure for the open configuration, as shown in the inset of Fig. 5, the field distribution remains nearly unchanged and the threshold gain increases only to about 145 cm^{-1} owing to the radiation losses. The quality factor of this open resonator without gain is Q=1125, whereas the values for the other 3D structures with a shield layer discussed above are even higher. Finally, we note that for electrical pumping, considerably higher gains may be reached [23], so that the structure, with appropriate changes, is expected to be even further reduced in size. In the following section we use the optimized thickness of a low index shield layer between the gain medium and the metal coating of a 3D laser resonator to experimentally demonstrate a nanolaser.

3.0 Room Temperature Lasing from Sub-wavelength Metallo-Dielectric Lasers

Previously, we have predicted that by incorporating a dielectric shield layer between the metal and the semiconductor (Fig. 6a, right) and optimizing the dielectric thickness, the gain threshold of the laser can be substantially reduced so that it is amenable to operation at room temperature [24]. The benefit stems from the tendency of the low-index shield to push the electromagnetic mode towards the high-index inner core and away from the metal walls, reducing the mode–metal overlap and hence the Joule loss. Excessive shield thickness can be detrimental, because the shield uses up space within the device that would otherwise be filled with the gain. For a fixed total waveguide radius R_{tot} and for each waveguide mode, an optimal shield thickness Δ (with the corresponding gain core radius $r_c = R_{tot} - \Delta$) exists that minimizes the threshold gain [24]. This is illustrated in Fig. 6b for the TE01 mode and R_{tot} = 460 nm (the same device footprint as in Fig. 1), using silica (n = 1.46) as the shield layer. It can be seen that the optimally sized shield ($\Delta \approx 200$ nm) reduces the gain requirement several fold relative to a metal-clad device of equal diameter but without the shield ($\Delta = 0$). Furthermore, one can ensure, by proper design, that the mode of interest is in cutoff in the upper and lower sections of the waveguide, where the core is only composed of dielectric with no high-index core (Fig. 6a). When this is the case, the structure acts as a 3D optical resonator [24].

The conceptual diagram in Fig. 6a implies that the upper and lower waveguide sections, where the mode is in cutoff, extend to infinity. In practice, we truncate the guide some distance above and below the gain section (Fig. 6c), far enough so that the energy leakage resulting from this truncation is minor. The light escaping from the lower section is used as the laser output, and the upper section is capped with metal for unidirectional emission and fabrication process compatibility. Also, owing to a selective etch step in our fabrication process, the lower cutoff section ends up comprising a composite core with an air column directly underlying the gain block (instead of a solid silica core). This does not compromise the performance of the resonator; in fact, it makes the cutoff in the lower section more severe. Figure 6d shows two cross-sections of $|\boldsymbol{E}|$ for the TE_{012} mode of the resonator in Fig. 6c. The resulting room temperature Q of this cavity is about 1030 (assuming gold (ε =-95.9-11i) for the metal shield), with a resonance at 1.55μm and a gain threshold of only 130cm^{-1}. Note that both the physical size and modal size of this cavity are smaller than the wavelength of emission. Assuming a minimum metal shield

thickness of 70 nm (which is twice the skin depth), the diameter and height of this laser are 1.1 and 1.35 mm, respectively. Also, in addition to having a low gain threshold, the laser is optically isolated from any structure placed next to it.

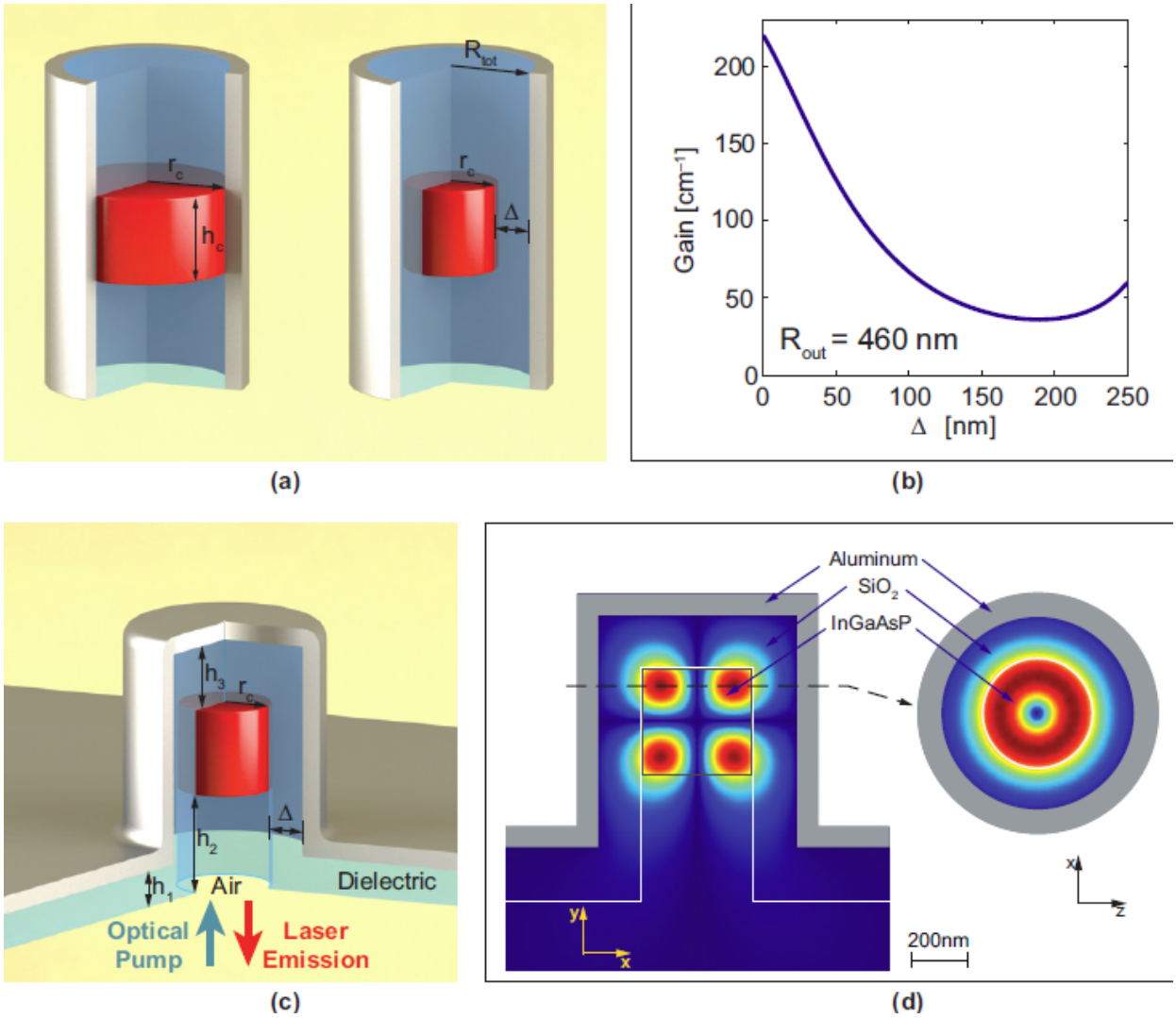

Fig. 6. (a, left) Metal coated gain disk with vertical confinement provided by low index waveguide cutoff sections. (a, right) The same structure but now including a dielectric shield layer with thickness Δ. (b) Variation of gain threshold of the composite gain/dielectric/metal waveguide as the dielectric shield thickness Δ is changed, assuming a fixed total radius R_{tot}=460nm. (c) Practical realization of the laser cavity for compatibility with planar fabrication techniques. The air gap at the bottom of the laser is formed after selective etch of the InP substrate. (d) Cross sections of $|\boldsymbol{E}|$ for the TE_{012} mode of the cavity. In the designed cavity the values for h_1, h_2, and h_3 are 200nm, 550nm and 250nm , respectively.

The shielded laser structure was fabricated from an InGaAsP MQW gain layer grown on InP. Hydrogen silsesquioxane (HSQ) electron-beam resist was patterned into arrays of dots (Fig. 7a)

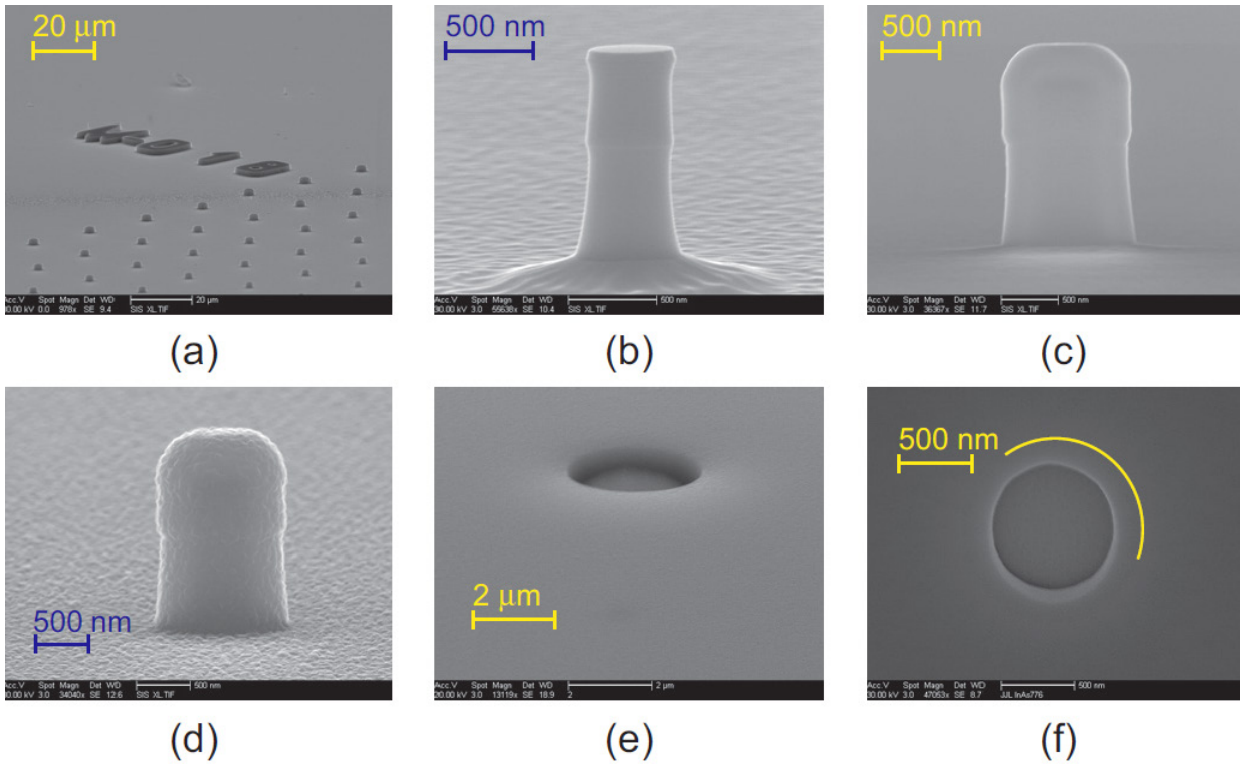

Fig. 7. Various stages of the fabrication process: (a) Array of e-beam patterned HSQ resist dots. (b) RIE etched pillar after oxygen plasma and BOE cleaning. The faint bump in the middle indicates the boundary between the InGaAsP and InP layers. (c) Etched pillar after PECVD of silica . The outline of the semiconductor pillar can be seen through the silica layer. (d) Silica covered pillar after undergoing aluminum sputtering (70nm). (e) Tilted bottom view of one of the samples after selective InP etch with HCL. The surface is comprised of the PECVD deposited silica. The hole corresponds to the air hole shown in the diagram of Fig. 6-d. (f) Contrast enhanced normal bottom view of a cavity. The circular outline around the air hole is due to the dielectric shield and agrees well with the target dielectric shield thickness of 200nm.

using a Raith 50 electron-beam writer, and the size of the dots was varied by changing the pattern size and/or the electron-beam dosage. Cylindrical structures were then etched using CH4/H2/Ar reactive ion etching (RIE) (Fig. 7b). Using an optimized and calibrated plasma-enhanced chemical vapour deposition (PECVD) process, the silica shield layer was grown to a thickness of ~200 nm (Fig. 7c) Note that the outline of the embedded gain core is visible through the silica layer. In practice, the low adhesion of gold to silica caused separation of the dielectric portion of the structure from the metal layer. Fortunately, aluminum exhibits better adhesion properties, and at the wavelength of interest its optical properties are very close to gold. (The cavity Q of the resonator with an aluminum coating (ε=-95.9-j11); [20] is 1,004, which compares with 1,030 for gold. A layer of aluminum with a minimal thickness of 70 nm was sputtered over the silica covered pillars (Fig. 7d). The sample was then bonded on the upper side to a glass slide

using SU-8, and the InP substrate was subsequently removed in a selective HCl etch, leaving an air void under the structure. Figure 7e shows the tilted bottom view of an air void, with the lower face of the gain core visible inside. Figure 7f shows the normal bottom view (with enhanced contrast levels) of a similar void. The faint outline of the silica shield is discernible in this image, verifying the 200 nm thickness of the shield.

For optical pumping we used a 1,064-nm pulsed fiber laser operating at a repetition rate of 300 kHz and a pulse width of 12 ns. The pump beam was delivered to the samples using a ×20 or ×50 longworking- distance objective, which also collected the emitted light. To estimate the amount of pump power absorbed by the core, a full three-dimensional finite-element analysis was carried out over a range of core sizes. Using a double 4-f imaging system in conjunction with a pump filter (Semrock RazorEdge long wavelength pass), the samples were imaged onto either an IR InGaAs camera (Indigo Alpha NIR) or a monochromator (Spectral Products DK480) with a resolution of 0.35 nm and equipped with a cooled InGaAs detector in a lock-in detection configuration. Owing to the electron-beam writing process, the samples were slightly elliptical. The major and minor diameters of the gain core for the particular sample under test were measured to be 490 and 420 nm, respectively. In Fig. 8a, the light-light curve corresponding to a laser emitting at 1430nm is shown (blue dots), which shows a slope change indicating the onset of lasing at an external threshold pump intensity of about 700W/mm^2. The same data set is shown in a log-log plot (Fig. 8a, red inset graph), with the slopes of different regions of operation indictated on the plot. The S shaped curve clearly shows the transition from the photoluminescence (PL) to amplified spontaneous emission (ASE) and finally into the lasing regime. Also shown in Fig. 8a are the emission patterns of the defocused laser image captured with the IR camera, corresponding to continuous wave (CW) (Fig. 8a-I) and pulsed (Fig. 8a-II) pumping situations. The average pump intensity in each case was approximately equal to 8W/mm^2.

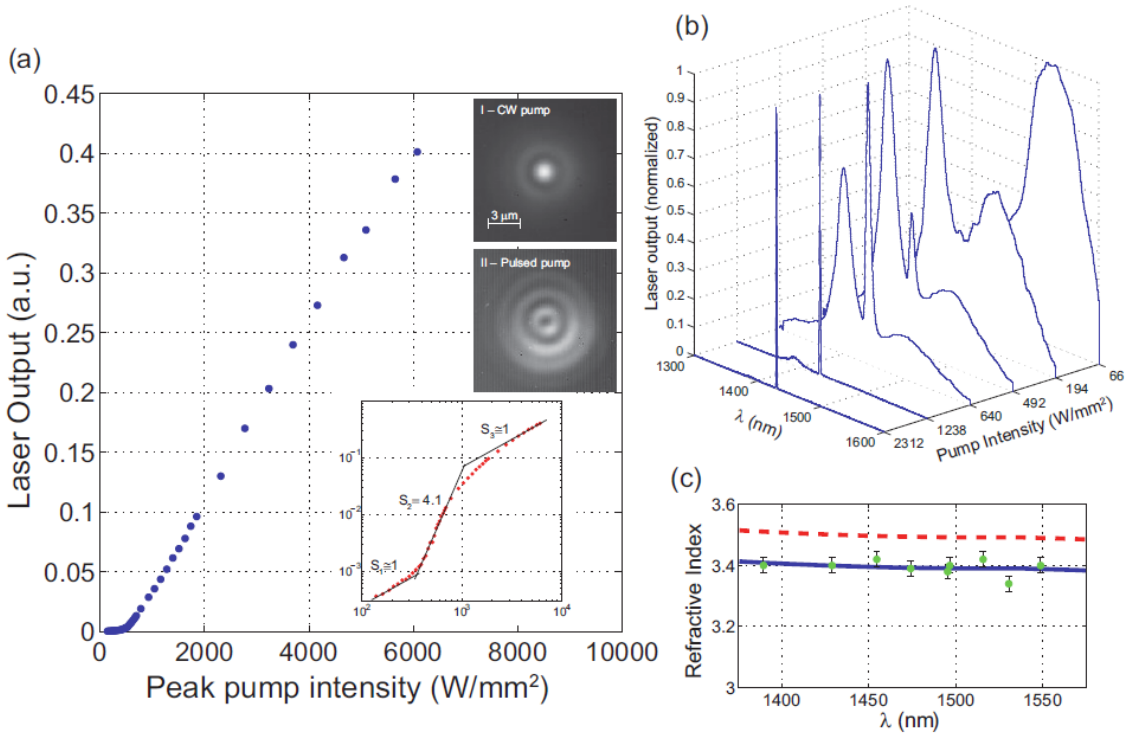

Fig. 8. (a) Light-light curve for a nanolaser with major and minor core diameters of 490nm and 420nm (blue dotted curve). The same data set is shown as a log-log plot (red dotted inset) together with the slopes for the PL, ASE and lasing regions. Also shown are the images of the defocused emitted beam cross section (taken at about 10 um away from the nanolaser exit aperture) for I) CW pumping and II) pulsed pumping. The appearance of the higher contrast fringes indicates increased coherence due to lasing. (b) Evolution of the emission spectra from PL to lasing. (c) Effective refractive indices (green data points) of the pumped MQW gain medium at lasing wavelengths, back-calculated from lasing spectra obtained from an array of nanolasers. Error bars were calculated assuming ±5nm error in measuring the disk diameters from the SEMs. The dashed red curve shows the effective refractive index of the unpumped MQW layer, as measured by a Filmetrics interferometric analyzer. The blue curve is offset down from the red by a constant amount (0.102 RIU) which was chosen for best fit to the lasing data. The index reduction is consistent with the estimated free carrier effects.

Only broad PL emission occurs in the CW case, owing to the low peak intensity. However, when the pump is switched to pulsed mode, lasing is achieved due to the 278-fold increase in peak power. At the same time, the defocused image forms a distinct spatial mode with increased fringe contrast, which is an indication of increased spatial coherency and is further evidence of lasing. The polarization of the emission has a strong linear component, which is due to the slight ellipticity of the gain core. Fig. 8b shows the evolution of the emission, from a broad PL spectrum to a pair of competing ASE peaks and finally into a narrow lasing line at 1430nm. The measured linewidth of this particular laser was 0.9nm, however linewidths as small as 0.5nm were measured for other samples in the same size range.

Another way to verify the soundness and accuracy of the design and fabrication processes is to match the lasing wavelength with the target resonance of the cavity. However, owing to the high pump intensity, the refractive index of the gain core can vary substantially from its quiescent value and this can considerably shift the lasing line from its target wavelength. Using the measured results from an array of lasers with slightly different sizes (which were measured individually using a scanning electron microscope, SEM) and exact three-dimensional finite-element modelling of each of the gain cores, the refractive index of the gain medium under pumping conditions was estimated at each lasing point (Fig. 8c, green symbols and error bars). Assuming a uniform drop over the spectrum of interest and using a least-squares fit of these data points, the estimated refractive index drop is ~0.102 refractive index units (RIU) (least-squares fit) lower than that reported by interferometric multilayer measurements of the unpatterned wafers under low illumination intensity (Fig. 8c, red dashed line). We attribute this shift to be mainly due to free carrier effects (a combination of bandfilling, bandgap shrinkage and free carrier absorption) whose net effect at the estimated carrier density (about 1.2×10^{19} cm^{-3} for a 520nm diameter core,) is expected to cause a refractive index drop of about 0.1 RIU. Also a slight additional contribution (at most -0.004RIU) may also be present due to compressive pressure on the gain cores, which is exerted by the thermal shrinkage of the aluminum layer after deposition in the sputtering chamber.

In summary, we have demonstrated room-temperature lasing from subwavelength metallo-dielectric resonators. In addition to reducing the size below the emission wavelength in all three dimensions, the metal layer isolates the cavity from its outer environment. Extending the current design approach to an electrically pumped structure may have practical applications such as dense optical interconnects [25] and laser arrays for optical trapping and manipulation of particles18, both of which are currently limited by the larger size and lateral coupling effects in vertical-cavity surface-emitting laser (VCSEL) arrays. It should be noted that a characteristic of this laser design is that it allows the placement of two coherent sources in very close proximity while allowing them to operate independently with no cros-coupling. According to the Rayleigh criterion, two point sources that are placed closer thanType equation here. $0.61\frac{\lambda}{NA}$ cannot be resolved into separate spots in the image plane (where λ and NA are the wavelength and the numerical aperture of the imaging system, respectively). This places an upper bound on the

maximum packing density of a free space optical interconnect system. For an imaging system with NA=0.8 and operating at 1.55μm, the Rayleigh distance is about 1.2μm. which is slightly larger than the minimum spacing achievable with this nanolaser (which is about 1.1 μm). Crossing the Rayleigh limit implies that arrays of this type of nanolaser can potentially reach the diffraction-imposed maximum bound on interconnect density. It should be stressed that passing this limit might also be advantageous for potential near-field applications that may benefit from further reduction in the nanolaser size. However, it should also be noted that due to the physical limits imposed on the size of resonators employing conventional reflective resonances (such as the current nanolaser design), using this approach to reduce the resonator dimensions to sizes far below $\lambda_0/2n$ (about 200nm, assuming λ=1550nm and n=3.4) is not feasible and the solution will most probably lie in the realm of plasmonic resonant devices, assuming that the high room temperature loss in such cavities can be efficiently surmounted. The small size of the cavity may also enable the implementation of high-speed directly modulated lasers through spontaneous emission enhancement by means of the Purcell effect [26]. Using silver instead of aluminium is expected to improve the threshold characteristics of these lasers because of its superior optical properties. In addition, given that the current resonator design is readily scalable to longer wavelengths (due to the improved optical properties of metals in the infrared), it may also be applied to develop planar arrays of metallo-dielectric quantum-cascade lasers that are integrated with metallic beam-forming elements [27] and can be used for high-resolution imaging in the mid- and far-infrared regions of the spectrum.

3.0 Electrically pumped sub-wavelength metallo-dielectric lasers

Dense integration of optoelectronic circuit and systems [28] will rely on construction of 3-D nanolaser devices with electrical injection to allow chip-level integration with existing electronic circuitry, ans at the same time provide minimal footprint and higher energy efficiency. The demonstrated nano-pillar laser design [8] had a high mode overlap with the metal coating and the high ohmic loss in the metal at optical frequencies limiting its operation only at cryogenic temperatures. Room temperature operation was reported when one of the cavity dimensions was expanded to a few wavelengths and gold was substituted with silver [29]. The demonstrated optically pumped subwavelength shielded metallo-dielectric cavity lasers discussed above[30] have the potential to exploit electrical injection and increase their operating temperature. The

high reflectivity of the metal in this design allows for efficient mode confinement while a thin low refractive index dielectric shield (SiO_2) between the gain and metal coating layer minimized the optical mode overlap with the metal coating [24]. As a result, the threshold gain can be significantly reduced, potentially enabling lasing at room temperature. The challenge is to design a composite metal-dielectric-semiconductor 3-D resonators with electrodes which simultaneously act as low effective index plugs of the 3-D laser cavity.

3. 1. Cavity Design and Modeling of Electrically pumped sub-wavelength metallo-dielectric lasers

The platform for our devices is based on an InGaAs/InP double heterostructure grown on an InP substrate similar to the structure reported in [8]. The schematic of the laser structure is shown in Fig. 9a. The intrinsic 300 nm thick (h_{core}) InGaAs bulk layer is the active layer and the upper (470 nm thick) and lower (450 nm thick) InP layers are the cladding layers through which the injected carriers are flowing into the active layer. Highly doped n-InGaAs on the top and p-InGaAsP in the lower cladding layer form the n and p contact layers, respectively. The top and bottom InP cladding width is intentionally reduced using selective wet etching to form a pedestal structure for enhancing the vertical optical confinement. Thin dielectric and metal layers are coated on the pillar structure which forms a metallo-dielectric cavity. We have previously reported that the metallo-dielectric cavity is able to achieve efficient lateral mode confinement in the subwavelength scale due to the high reflectivity of the metal while reducing the optical ohmic loss by minimizing the mode overlap with the metal using a thin dielectric shield [30,24]. COMSOL multiphysics was used for 3D FEM modeling of our structure. The dielectric constant of bulk silver at room temperature ($\varepsilon_{Ag} = -120.43 - i3.073$ at 1.55 μm) was used for the metal coating [9]. We first designed the wavelength scale cavity in which the gain core radius (r_{core}) is 750 nm ($2r_{core} \sim \lambda$), the cladding radius (r_{clad}) is 690 nm (Δr = 60 nm) and SiO_2 shield thickness (d_{shield}) is 150 nm. The electric field intensity of the resonant cavity mode was calculated and the field intensity (horizontal cross-section) in the gain medium is shown in Fig. 9b. The whispering gallery mode (WGM) with the azimuthal mode number (M) of 7 is supported and the electric field is strongly confined inside the metal cavity (TE mode). The thin active layer (h_{core} =300 nm) allows only the lowest order mode in the vertical direction. The mode overlap with the metal coating is minimized by the dielectric shield as shown in Fig. 9b. As the dielectric shield

becomes thinner, the field penetration into the metal coating is increased which results in a higher loss. In contrast, a thick dielectric shield could reduce the field penetration into the metal, however, the relative ratio of gain in the whole structure is decreased which eventually results in a lower gain. Therefore, there should be an optimum thickness of the dielectric shield for given gain core radius.

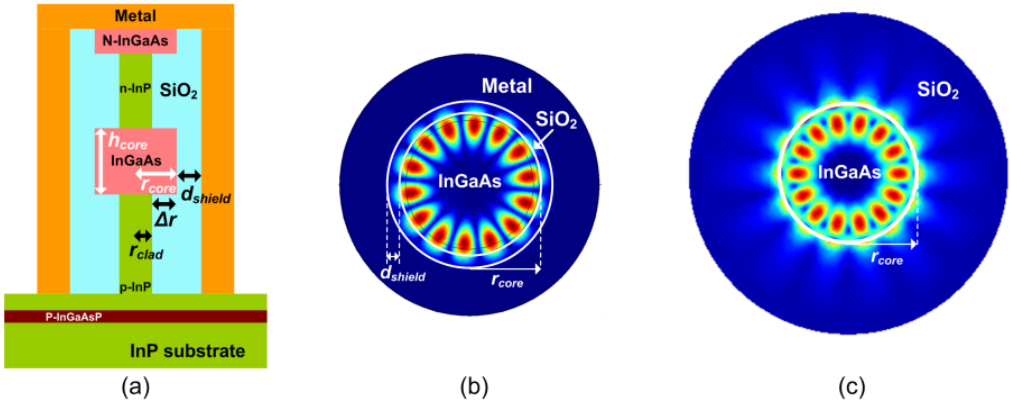

Fig. 9. A schematic of subwavelength pedestal pillar laser shown in (a) where r_{core} is the radius of InGaAs gain layer, r_{clad} is the radius of InP cladding. Δr is the difference between r_{core} and r_{clad}. d_{shield} is the thickness of SiO_2 shield layer. h_{core} is the height of InGaAs gain medium. (b) The horizontal cross section of the electric field intensity when r_{core} is 750 nm, r_{clad} is 690 nm (Δr=60 nm), and d_{shield} is 150 nm with silver coating. (c) The horizontal cross section of the electric field intensity in the same structure with only low index dielectric (SiO_2) coating. r_{core} in (b) and (c) are the same as 750 nm.

For comparison, we numerically modeled the same pedestal structure coated only by a low index dielectric (n_{SiO2}=1.45) without a metal coating. The electric field intensity of the resonant mode of this dielectric cavity is shown in Fig. 9c. It shows significant mode spreading outside the gain medium which results in low mode overlap with the gain medium. In our calculation, the confinement factor in the gain medium of the metallo-dielectric cavity (Fig. 9b) is 0.39 compared to 0.19 in the pure dielectric cavity case (Fig. 9c). The Q factor of metallo-dielectric cavity is 726 which is a factor of 5 enhancement from the Q factor of the dielectric cavity (Q = 151). When the gain core size is decreased below the wavelength scale, the confinement factor is significantly degraded due to the radiation loss which was studied in the micro-disk resonators [31,32]. Figure 10a shows the resonant mode of a pure dielectric cavity where r_{core} = 350 nm and r_{clad} = 310 nm (Δr=40 nm) with the low index dielectric (SiO_2) coating. This structure supports WGM with M = 3 exhibiting a significant mode spreading outside the gain medium and a low confinement factor in the gain medium (0.38).

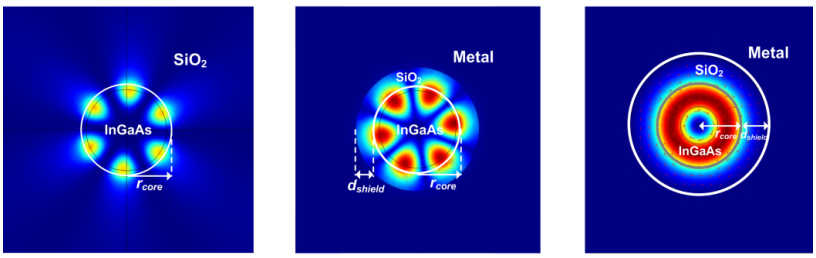

Fig. 10. The electric field intensity at the horizontal cross section of the active layer. (a) pure dielectric cavity with r_{core} = 350 nm, r_{clad} = 290 nm (Δr=60 nm), and SiO_2 coating. (b) metallo-dielectric cavity with r_{core} = 350 nm, r_{clad} = 290 nm (Δr=60 nm), d_{shield} = 150 nm, and Ag coating. The gain structure sizes, r_{core} and r_{clad}, in (a) and (b) are the same and the resonant mode is WGM with M=3 for both cases. (c) metallo-dielectric cavity with r_{core} = 220 nm, r_{clad} = 160 nm, d_{shield} = 150 nm, and Ag coating. The resonant mode is axially symmetric TE_{011}.

However, by incorporation of the metallo-dielectric cavity (150 nm thick SiO_2 and Ag coating) as shown in Fig. 10b, the resonant mode is strongly confined inside the subwavelength scale cavity and the mode overlap with the gain is also significantly enhanced. In our calculation, the confinement factor in the gain medium in metallo-dielectric cavity is 0.57. Thus for such small size resonators, this results in a factor of 22 improvement in the Q factor of metallo-dielectric cavity (Q = 468) compared to the Q factor of the pure dielectric cavity (Q = 21). Metallo-dielectric cavity enables further reduction of the gain core size while keeping efficient mode confinement in the gain medium. We numerically calculated the resonant mode of the metallo-dielectric cavity with r_{core} = 220 nm, r_{clad} = 160 nm (Δr = 60 nm) and d_{shield} = 150 nm. As shown in Fig. 10c, for this case, the resonant mode is an axially symmetric mode (TE_{011}) for which the electric field is circulating around the gain core and is well-confined in the gain medium. The electric field intensity is mostly contained inside the gain medium with minimal mode overlap with the metal region. The Q factor of this resonator is calculated to be 707 with the threshold gain of 236 cm^{-1} which is lower than InGaAs bulk gain (400 cm^{-1}) at room temperature at 1.5 μm [33]. The pedestal geometry is adopted in our metallo-dielectric cavity pillar laser structure to enhance the optical confinement in vertical direction while maintaining a conduit for carrier flow of both electrons and holes. To quantitatively analyze the effect of the pedestal in our laser structure, we calculated the Q factor and the threshold gain by varying r_{clad}.

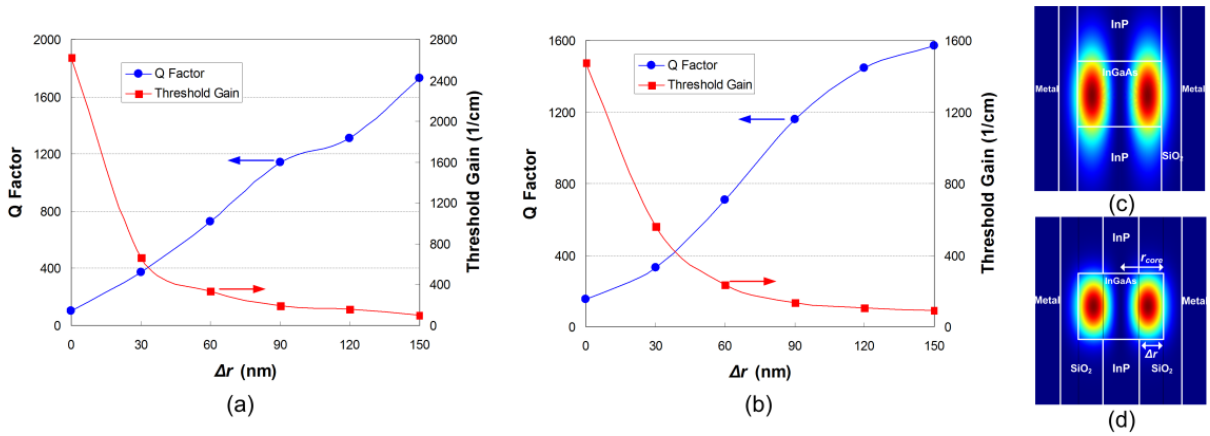

Fig. 11. Numerical simulation results of the cavity Q factor and threshold gain for various pedestal sizes. Δr (= r_{core} - r_{clad}) is pedestal undercut depth. (a) r_{core} = 750 nm, d_{shield} = 150 nm, and r_{clad} is varied from 750 nm to 600 nm (Δr = 0 ~ 150 nm). Blue curve represents the cavity Q and red curve for the threshold gain. (b) r_{core} = 220 nm, d_{shield} = 150 nm, and r_{clad} is varied from 220 nm to 70 nm (Δr = 0 ~ 150 nm). (c) Vertical cross section of the resonant mode field (TE_{011}) intensity when r_{core}, r_{clad} = 220 nm (Δr =0 nm, cylinder type), and d_{shield} = 150 nm. (d) The resonant mode field (TE_{011}) intensity when r_{core} = 220 nm, r_{clad} = 100 nm (Δr =120 nm, pedestal type), and d_{shield} = 150 nm.

The calculated Q factor and threshold gain for 750 nm core radius with various r_{clad} is presented in Fig. 11a. Shield thickness (d_{shield}) and the metal coating were kept constant. When r_{clad} is the same as r_{core} (cylinder type), the Q factor is 163 and the threshold gain is 1505 cm^{-1}. As r_{clad} is reduced to 600 nm (pedestal type, Δr = 150 nm), the Q factor is enhanced to 1731 which is about an order of magnitude improvement and the threshold gain is decreased to 99 cm^{-1} which is 93 % reduction. As the pedestal undercut is made deeper (Δr is larger), the threshold gain is flattened and the resonant wavelength is shifted out of the optimal gain spectrum which is not desirable. We also calculated the Q factor and threshold gain when r_{core} = 220 nm with changing the pedestal size which is shown in Fig. 11b. The Q factor is enhanced from 152 (cylinder type, Δr = 0 nm) to 1572 (pedestal type, Δr = 150 nm) which is an order of magnitude improvement. The resonant mode is strongly confined inside the gain layer with pedestal structure as shown in Fig. 11d where r_{core} = 220 nm and Δr = 120 nm compared to the cylinder type structure shown in Fig. 11c. The threshold gain is reduced from 1473 cm^{-1} to 89 cm^{-1} which is 94 % reduction. The threshold gain of 89 cm^{-1} is a promising result for possible room temperature operation of this laser structure. As shown in both cases, the threshold gain is significantly suppressed with minimal pedestal undercut. At Δr =60 nm, the threshold gain of 750 nm and 220 nm r_{core} are 338 cm^{-1} and 236 cm^{-1}, respectively, which are still lower than our target threshold gain of 400 cm^{-1} [33]. This is another advantage since heat dissipation and carrier diffusion in the active layer have been critical issues for most pedestal type micro-disk lasers [34,35].

3. 2. Fabrication of electrically pumped sub-wavelength metallo-dielectric lasers

The wavelength scale (750 nm radius) and sub-wavelength scale (355 nm radius) circular masks on InGaAs/InP heterostructure wafer were patterned by the e-beam lithography on the spin-coated hydrogen silsesquioxane (HSQ) resist. Subsequent dry etching was performed using CH_4:H_2:Ar gas chemistry to form the subwavelength scale pillar structure (the scanning electron microscopy (SEM) micrograph is shown in Fig.12a). The selective etching of the cladding InP layers was performed using HCl:H_3PO_4 (1:3) wet etching and the result of which is shown in Fig. 12b. 160 nm of InP was etched on both sides through the wet etching process while the gain layer was preserved. 150 nm of SiO_2 layer was conformally deposited on the pedestal pillar surface by PECVD process which both provides the low index shield minimizing the mode-metal overlap and passivates the InGaAs surface.

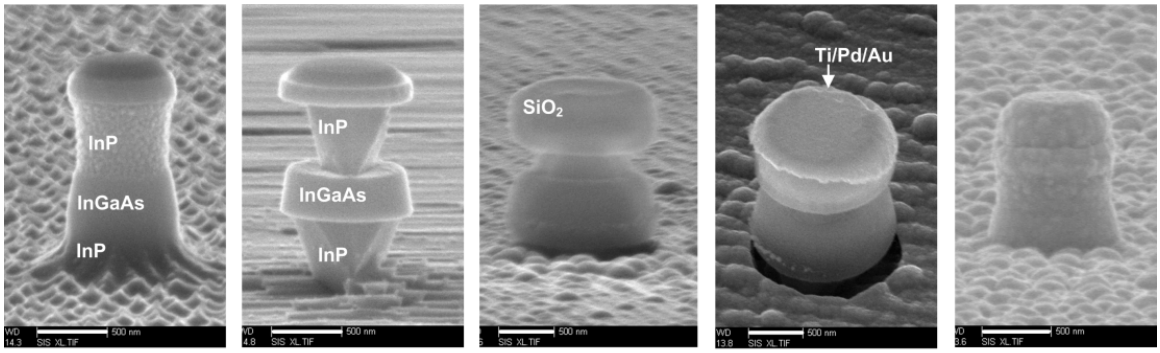

Fig. 12. SEM micrographs of subwavelength pillar laser structure during fabrication procedure. (a) Subwavelength pillar (r_{core}= 395 nm) structure after dry etching. (b) Pedestal pillar is formed by selective InP wet etching. (c) Thin SiO_2 layer (140 nm) is deposited on the pillar structure by PECVD. (d) N-contact metal (Ti/Pd/Au) layer deposited on the top of subwavelength pillar. (e) Silver is deposited on whole pillar structure. Scale bar in each image represents 500 nm.

The SiO_2 layer on the top of the subwavelength pillar structure was removed through the photoresist planarization and SiO_2 dry etching to access the n-side contact layer (n-InGaAs). Metal contacts (Ti/Pd/Au) were formed on the top of the pillar structure by the e-beam evaporation and lift-off (Fig. 12d). After n contact formation, a 200 nm thick silver layer was deposited to cover the whole pillar structure including the top and side wall of the pillar and n contact pad (Fig. 12e). A 20 nm thin chromium (Cr) layer was deposited prior to the silver deposition for better adhesion. Since a high optical loss of Cr could degrade the Q factor of the cavity and therefore increase the threshold gain, the unintentionally deposited Cr on the side wall of the pillar structure was subsequently removed by Cr wet-etching while protecting the adhesion

layer on the substrate by the photoresist masking. P-contact was separately processed by the photolithographic patterning and wet-etching of SiO_2 and InP layer to access the underlying highly doped InGaAsP layer. The sample was then annealed to 400 ºC for 60 s to reduce the contact resistance. Finally, the sample was mounted on the device package (TO 8) and wire-bonded.

3. 3. Measurements and Discussion of electrically pumped sub-wavelength metallo-dielectric lasers

The devices were forward biased and the continuous wave (CW) emission from the device was collected through a 20× objective lens and then imaged by the CCD camera. The spectral characteristics were analyzed by the monochromator with a maximum spectral resolution of 0.35 nm (with a 100 μm slit opening). The lasing characteristics of electrically pumped pedestal pillar lasers with two gain core radii (750 nm and 355 nm) were measured and analyzed. Figure 13a shows a SEM micrograph of the pedestal pillar in which r_{core} = 750 nm, r_{clad} = 710 nm with 1.3 μm pillar height. The shield thickness (d_{shield}) was 140 nm and silver was coated as a metal cavity. In the numerical simulation, the Q factor was estimated to be 458 and the threshold gain was 534 cm^{-1} at the resonant wavelength of 1.50 μm. The lasing characteristics of this device at 77 K are shown in Fig. 13b. Electroluminescence (EL) around 1.55 μm was observed when the injected current was higher than 20 μA. As the injected current was increased, the emission spectrum showed a spectral narrowing and the lasing peak appeared at 1.49 μm which is very close to the calculated resonant wavelength of 1.50 μm. The light output-injection current (*L-I*) curve (Fig. 13c) shows the kink around the threshold current (50 μA) which is also an indication of the onset of lasing. The linewidth narrowed to 0.9 nm with the injection current of 300 μA. We also investigated the temperature dependence of the lasing characteristics of this device. A local heater inside the cryostat kept the target temperature constant during the measurement. Lasing behavior was observed at 100 K, 120 K and 140 K with constant current pump. The spectral evolution and *L-I* curve at 140 K is shown in Fig. 13e. The lasing wavelength remains in the vicinity of 1.49 um and the linewidth was also less than 1 nm at 140 K. However, the threshold current increased to 240 μA (inset in Fig. 13e) which is 5 times higher than the threshold current at 77 K. At 160 K, spectral narrowing at 1.49 μm is still observed but failed to

reach lasing primarily due to the heat generation inside the cavity and the higher optical loss in metal cavity.

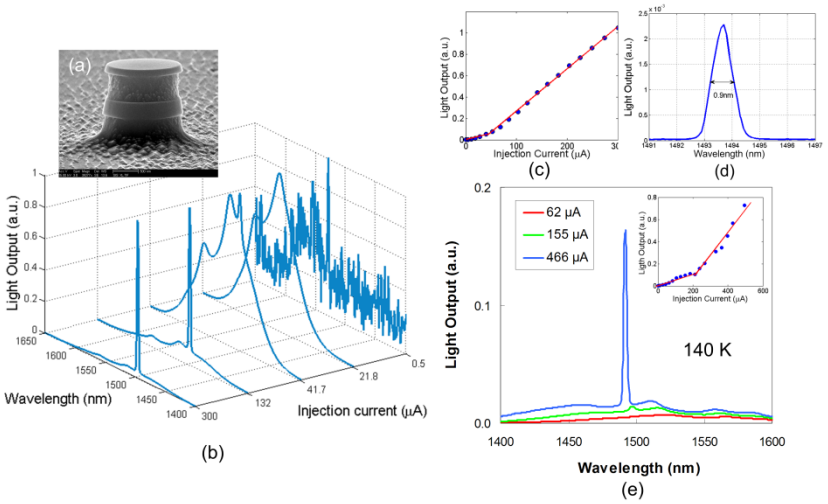

Fig. 13. Lasing characteristics of 750 nm r_{core} pedestal pillar laser device. (a) An SEM micrograph of 750 nm r_{core} pedestal pillar structure. (b) Spectral evolution graphs with increasing the injection current. (c) *L-I* curve of this device. (d) Linewidth measurement by a monochromator with 0.35 nm resolution. (e) Lasing spectrum measured at 140 K. Inset shows *L-I* curve at 140 K.

The lasing characteristics of 355 nm core radius subwavelength pillar laser were also investigated as shown in Fig. 14. An SEM micrograph of the pedestal pillar structure is shown in Fig. 14a. The pillar structure had r_{core} = 355 nm, r_{clad} = 310 nm, d_{shield} = 140 nm with 1.36 μm pillar height and silver coating. As discussed in the numerical simulation, this cavity structure supports the WGM with M = 3. From the simulation, the Q factor was estimated at 352 and the threshold gain was 692 cm^{-1} at the resonant wavelength of 1.38 μm. As shown in Fig. 14b, the spectral narrowing was observed as injection current was increased and the lasing peak occurred at 1.41 μm. The threshold current was estimated around 540 μA which is 10 times higher than for the 750 nm r_{core} device due to the lower material gain at shorter wavelengths and higher threshold gain. The resonant wavelength from the simulation (1.38 μm) matches the measurement results quite well. Higher resolution analysis of the lasing peak spectrum showed that the lasing peak at 1.41 μm is a dual peak with 1.5 nm splitting (Fig. 14d, which indicates the imperfect circular symmetry of the pillar structure due to fabrication. When the temperature is increased, the CW lasing operation was observed up to 100 K. As shown in Fig. 14e, the onset of the lasing peak is clearly observed and the linewidth is about 6 nm at 100 K. At 120 K, the output spectrum showed clear spectral narrowing with 8 nm linewidth which indicates the cavity

mode, but failed to reach lasing which could be due to the heating from the high driving current. It is expected that pulsed operation could reduce the heating issue so that the device could operate at even higher temperatures. Based on our numerical simulation above, a smaller size (r_{core}= 220 nm) device should be able to be lase with a low threshold gain (< 100 cm^{-1}). However, the fabrication difficulties such as forming pedestal structure on 200 nm width InP cladding with the wet etching process are still challenging and the thermal management becomes even more critical with subwavelength scale pillar widths. We are currently working on resolving these issues by optimizing our fabrication process and developing a low resistance contact design which could reduce the electrical power dissipation and self-heating in the device. Incorporation of quantum well or quantum dot gain structures in our laser devices could also allow for building highly efficient subwavelength-scale lasers [30,36].

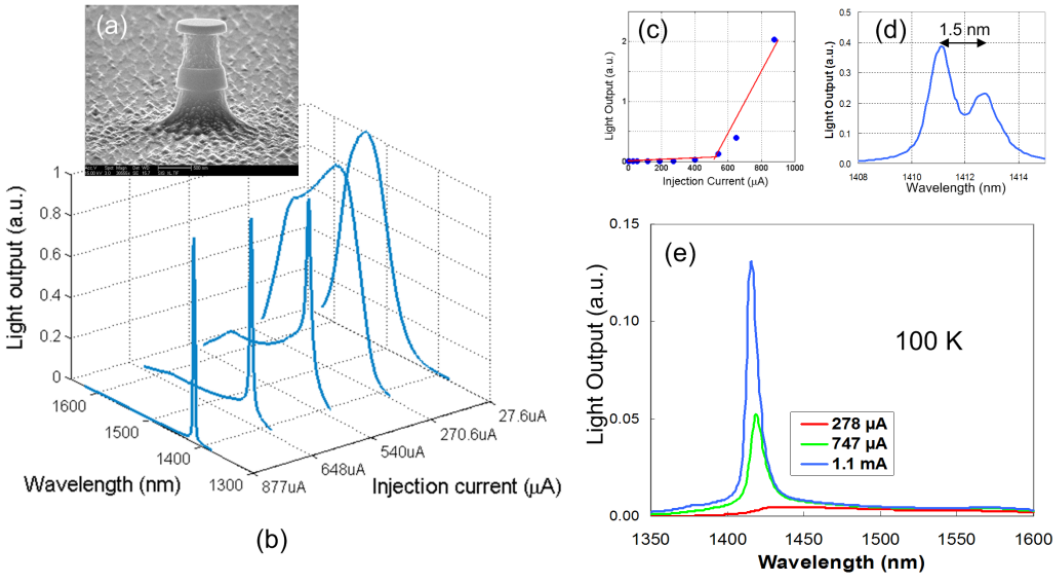

Fig. 14. Lasing characteristics of 355 nm r_{core} pedestal pillar laser device. (a) An SEM micrograph of 355 nm r_{core} pedestal pillar structure. (b) Spectral evolution graphs with increasing the injection current. (c) *L-I* curve of this device. (d) Linewidth measurement by a monochromator. (e) Lasing spectrum with difference injection currents measured at 100 K.

In summary, we have demonstrated a new design and fabrication of wavelength- and sub-wavelength scale electrically driven lasers using metallo-dielectric cavities. In the design, the metal cavity combined with thin low index dielectric layer enabled a significant enhancement in mode confinement for both wavelength and subwavelength scale cavities. Using a pedestal geometry improved the vertical mode confinement and showed a huge reduction in the threshold gain with increasing undercut in pedestal cladding. To lower the threshold gain below the target

400 cm^{-1}, it requires a minimal undercut (< 60 nm) in the pedestal for 750 nm and 350 nm core radius laser. This is a clear advantage for efficient heat transfer and carrier diffusion in the active region. In the experiment, we present the fabrication process for our designed structure based on InGaAs/InP double heterostructure. Laser devices were fabricated for 750 nm and 355 nm gain core radii. We observed a clear lasing operation at 77 K for both laser devices with low threshold current of 50 μA and 540 μA, respectively. For the r_{core} =750 nm laser device, the CW lasing operation at 1.49 μm was observed up to 140 K. The r_{core} =355 nm laser device showed the CW lasing operation up to 100 K. Numerical studies suggest that even smaller laser structures (core radius = 220 nm) could exhibit low threshold gain which is also feasible for room temperature operation.

4. 0. Wafer Bonded Silicon-III-V Sub-Wavelength Metallo-Dielectric Laser

Realization of silicon photonics compatible active optical components is critical for creating integrated silicon photonic circuits, and a major step towards integration with CMOS-compatible platforms. Silicon has good thermoconductive properties, high quality oxide, low cost, and is available in high quality wafers, making it invaluable for integrated electrical circuits and waveguides. Unfortunately, the indirect bandgap of silicon poses a fundamental barrier to enabling light amplification and stimulated emission in this material. Successful advances toward overcoming this limitation include demonstration of silicon Raman lasers [37] and light emission in silicon-based nanoengineered materials [38]. However, Raman laser operation is based on optical scattering, which makes it essentially limited to operation under external optical pumping. Silicon nanostructures, in turn, suffer from low gain, and therefore, low efficiency.

An alternative solution is to build hybrid optical devices through integration of III-V gain with silicon [39] using wafer bonding. III-V semiconductor compounds offer the benefits of a direct energy bandgap with wide achievable range, and high carrier mobility. This makes the III-V material system optimal for active optical elements and logical devices such as lasers, switches, and modulators. In addition to integration with silicon, another major goal of current photonics research is to reduce device footprints. Miniaturization is of great importance for the realization of compact photonic circuits for optical interconnects on-chip optical communication, and sensing. Many applications often require high density packaging of laser structures, and therefore three dimensional minimization of the lasers is ultimately desired. To date, several

different subwavelength lasing structures were demonstrated by a few research groups [8,40-43], but integration of sub-wavelength lasers with passive silicon photonics still remains a challenge.

Earlier we demonstrated room-temperature sub-wavelength metallo-dielectric lasers [30], where the dielectric shield between metal cavity and gain core allows us to achieve lasing at room temperature through metal loss reduction [24]. However, building a practical ultra-compact on-chip device prompts us to address a few issues that include integration of the optical gain material with a silicon–on-insulator (SOI) wafer, assembly of an electrically injected laser cavity and laser-to-waveguide mode coupling. In the original design, the nanolaser is optically pumped and mounted on a glass slide with the output light propagating in free space (Figure 15a). The wafer bonding approach offers a path to realization of an electrically pumped sub-wavelength laser with vertical mode coupling to a silicon photonic waveguide by means of a slanted mirror, for example [35].

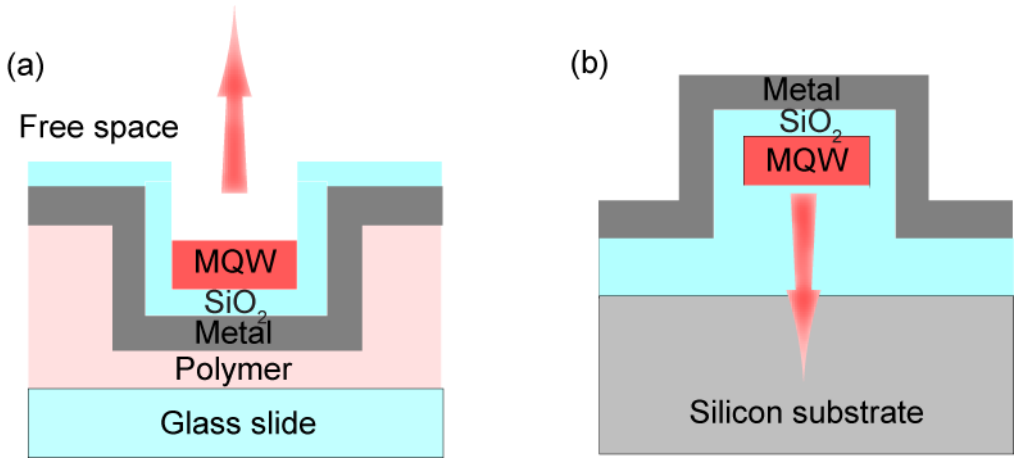

Fig. 15. (a) Scheme of the original sub-wavelength metallo-dielectric laser setup; (b) scheme of a wafer bonded metallo-dielectric laser.

In order to exclusively investigate wafer bonding problems, we choose to keep the original cavity mode of the optically pumped nanolaser [30] intact. Thus, the III-V-to-silicon wafer bonding has to be mediated by low refractive index material, such as SiO2, to achieve vertical mode confinement (Figure 15b). The mediator layer has to be thick enough to reproduce the 500nm air plug in the original design. Next, we need to select a reliable and versatile wafer bonding method, which could be used for both III-V-to-Si and III-V-to-SiO2/Si integration.

The wide variety of available wafer bonding techniques includes fusion bonding, anodic bonding, solder bonding, eutectic bonding, thermocompression bonding, direct metal-to-metal bonding, ultrasonic bonding, low-temperature melting glass bonding, and adhesive bonding [44]. Our choice was determined by the cavity design, which required a direct low temperature (below 400°C) bond of an InGaAsP multiple quantum well (MQW) active layer to a silicon base. Conventional high temperature direct wafer bonding (fusion bonding) is known to have an adverse effect on the III-V layer quality due to a thermal expansion constant mismatch of the bonded materials. Some of the available low temperature wafer bonding methods may be useful, but would require additional studies of the bonding mediator's optical and material properties (adhesive wafer bonding), its possible chemical interaction with the gain layer (anodic wafer bonding) and incorporation of these new layers into the original nanolaser model.

Recently, Liang at al reported a plasma assisted wafer bonding method,[45, 46] which they successfully used for realization SOI-compatible optoelectronic devices [39]. Hence, in this work we demonstrate a silicon-compatible metallo-dielectric nanolaser and investigate the feasibility of this fabrication approach for integration of the nanolasers with silicon photonics platform.

4. 1. Design and Simulations of Wafer Bonded Silicon-III-V Sub-Wavelength Metallo-Dielectric Laser

Microdisk resonators with conventional whispering gallery mode (WGM) designs can be reduced to subwavelength scale [5], but the corresponding mode for the small structure is loosely bound, such that its evanescent tail is spread far beyond the physical resonator boundaries. This creates two problems. First, it increases the threshold requirements since the mode/gain overlap is reduced. Second, coupling between the modes of neighboring resonators makes the WGM resonators unsuitable for densely packed laser arrays. These issues can be solved by enclosing the semiconductor resonator in a metal cavity [8]. While the metal cavity introduces strong mode confinement and thereby increases the mode/gain overlap, it also introduces high Joule losses. The last circumstance poses a difficulty on the way to room temperature lasing in subwavelength metallic resonators. Our approach to overcoming the metal losses is to incorporate a dielectric shield layer between the metal and semiconductor [24]. The shield thickness can be optimized for a fixed outer diameter of the laser. For an optimum shield thickness the losses reduce such

that threshold gain is small enough for room temperature operation. In this case, we are still benefiting from the metal confinement, but the dielectric shield separates the largest portion of the mode, concentrated in the high index gain core (~ 3.5 for bulk InGaAsP), from direct interaction with the metal. Excessive shield thickness is detrimental, because the dielectric layer takes space that could otherwise be filled with the gain medium. Here we attempt to adapt this approach for an InGaAsP MQW gain layer, wafer bonded to SiO2/Si (silicon wafer with thermally grown silicon dioxide layer), using our original design for the InGaAsP/InP material system. Figure 16a shows a schematic of a sample metallo-dielectric nanolaser, optimized for minimum lasing threshold at a nominal wavelength of 1550nm and outer radius of the resonator Rout=460nm. For a structure for these dimensions, the optimized shield thickness (Δ) and gain core radius (Rcore) are 200nm and 250nm, respectively [24]. The gain core of the laser consists of InGaAsP with MQW (the actual composition of the gain layer is summarized in Table 1).

Name	Material	Thickness(A)	Number of layers
Capping layer	InP	100	1
Active region	1.3 Q In_xGa_{1-x} As_yP_{1-y}	200	16
	1.6 Q In_xGa_{1-x} As_yP_{1-y}	100	16
	1.3 Q In_xGa_{1-x} As_yP_{1-y}	200	1
Substrate	InP	~325 micron	

Table 1. Multiple quantum well InGaAsP/InP epitaxial structure.

A layer of metal (silver) confines the electromagnetic fields within the cavity. The gain is separated from the metal by a shield layer of low-index dielectric (SiO2). The dielectric regions with low effective index above and below the gain cylinder ("plugs") provide vertical confinement of the resonator mode, as the lasing mode is in cutoff there. The lower plug is comprised of thermal SiO2, in contrast to the original air plug from our previous work. This setup does not introduce any significant changes in the design, since the refractive index of SiO2 is only slightly higher (1.46 versus unity for air). Finite element method (FEM) simulation of the laser resonator is shown in Figure 16b. The dielectric layer has been optimized for the TE012 mode, which has higher wavelength cutoff compared to the other lower order modes, but has the lowest achievable threshold gain of 36 cm-1 for the designed structure [24].

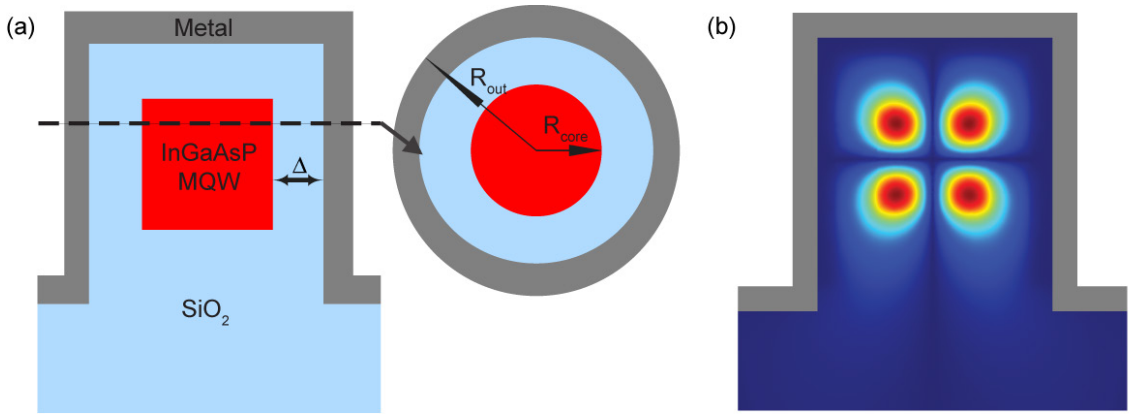

Fig. 16. Schematic drawing of the wafer bonded metallo-dielectric resonator design; b) FEM simulation of TE021 mode in metallo-dielectric resonator with Rout=460nm, optimized for 1550nm wavelength.

4. 2. Fabrication of Wafer Bonded Silicon-III-V Sub-Wavelength Metallo-Dielectric Laser

The wafer bonded sub-wavelength metallo-dielectric structures are fabricated from an InGaAsP multiple quantum well gain layer, bonded to a silicon wafer with a SiO2 layer on top. The complete fabrication scheme is outlined Figure 17. The silicon wafers have a 6μm thermally grown oxide layer on the surface. The MQW InGaAsP/InP wafer was ordered from OEpic Semiconductor, Inc. This gain layer is comprised of 16, 10nm thick, wells (1.6Q InxGa1-xAsyP1-y , x=0.56, y=0.938) embedded in 17, 20nm thick, barriers (1.3Q InxGa1-xAsyP1-y, x=0.734, y=0.571), epitaxially grown on an InP substrate, ~500nm thickness in total (Table 1). InGaAsP MQW active layer bonding to the SiO2/Si was accomplished through low temperature plasma assisted wafer bonding (Figure 17 a-c). The process is adapted from the III-V-to-Si bonding procedure recently developed by Liang et al [45, 46] and is described below.

The wafer bonding is performed for an InGaAsP/InP chip of ~ 1cm2 area and a SiO2/Si chip of ~ 2cm2 area. The low temperature bonding starts with ultrasonication of the cleaved wafers in solvents to remove all particles that would inhibit interaction between the surfaces. InGaAsP/InP is dipped in HCl for 10s prior to the wafer bonding to remove the InP capping layer. Ultrasonication in acetone and isopropanol (IPA), followed by thorough DI water rinse are necessary to eliminate particles from the bonding surfaces. This is a crucial step, since a single 1μm size particle results in an unbonded area of 1cm2 [47]. Next, the surfaces are to be stripped of native oxides, organic, and ionic contaminations. The chemical treatment is performed using

standard RCA clean (NH4OH:H2O2:H2O=1:2:10) for 10 minutes at 65–75°C on the InGaAsP/InP chip, and modified RCA clean (HCl: H2O2:H2O =0.2:1:5) for 10 minutes at 80°C on the SiO2/Si chip. Then, the InGaAsP/InP chip is immersed into NH4OH to remove any native oxides and small contaminations left from the previous step, while SiO2/Si is treated in H2SO4:H2O (3:1) for 10 minutes to strip any traces of organic contaminants.

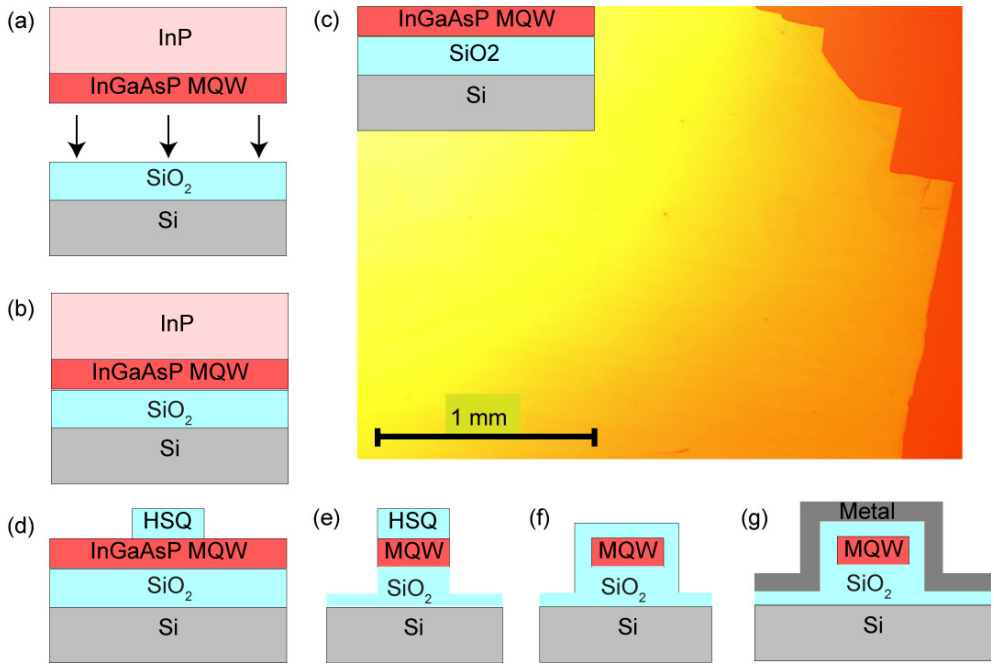

Fig. 17. Fabrication steps of a wafer bonded metallo-dielectric laser: a) wafer bonding of InGaAsP to SiO2/SI, b) resultant InP/InGaAsP/SiO2/Si structure, c) wet etching of InP substrate and the optical microscope image of 500nm InGaAsP MQW layer bonded to SiO2 /Si chip; d) e-beam lithography patterning; e) laser pillar after two step RIE of InGaAsP and SiO2 ; g) PECVD of SiO2 shield; h) metal sputtering (silver).

The chemical clean is followed by ultrasonication in acetone, IPA, careful DI water rinse and drying in N2 flow. After cleaning, both chips undergo O2 plasma surface activation in a Trion reactive ion etch (RIE) chamber with 20mTorr pressure, 30sccm O2 flux and 50W RF power for 45 seconds. The oxygen plasma treatment is immediately followed by a brief rinse in DI water to passivate the active surfaces with hydroxyl (–OH) groups. The water flow also takes away any new particles that may have accumulated during the plasma activation. Next, nitrogen flow-dried chips are manually mated. The Van der Waals force between the –OH groups promotes spontaneous mating of activated surfaces. The pair is annealed for 17 hours at 300°C in an oven to form strong covalent bonding and encourage out-diffusion of the H2O and H2 byproducts through the thick SiO2 layer from the InGaAsP/SiO2 interface. Lastly, the InP carrier substrate is

selectively etched by HCl from the bonded sample to obtain the composite InGaAs/SiO2/Si structure (Figure 17c).

The next step is to perform a double step reactive ion etch (RIE), which has to be carried out on the gain layer and SiO2 using appropriate etching chemistry for each of the two materials. E-beam lithographic processing was performed on hydrogen silsesquioxane (HSQ) negative resist to create a mask (Figure 17d). This is followed by the two-step RIE to form the cylindrical gain core and bottom SiO2 plug. First, the 500nm thick InGaAsP MQW layer is dry etched in CH4/H2/Ar (4:40:20sccm) chemistry. Then the SiO2 layer undergoes CHF3/Ar (25/25sccm) RIE to obtain a 500nm tall SiO2 post (Figire 17e depicts a schematic drawing of the structure after both these steps are performed). The HSQ mask is removed during the last fabrication step along with SiO2, since its chemical composition is quite similar to that of SiO2. Next the sample is treated in microwave oxygen plasma (Tepla 100) to eliminate polymer buildup. An SEM image of a sample laser after the cleaning is presented in Figure 18a. Next, PECVD of 200nm thick SiO2 is carried out to form the low index shield around the InGaAsP core (Figure 17f). Corresponding SEM image is shown on Figure 18b. In the final step we sputtered silver using a Denton Discovery 18 sputterer on the sample to complete a laser cavity (Figure 17g).

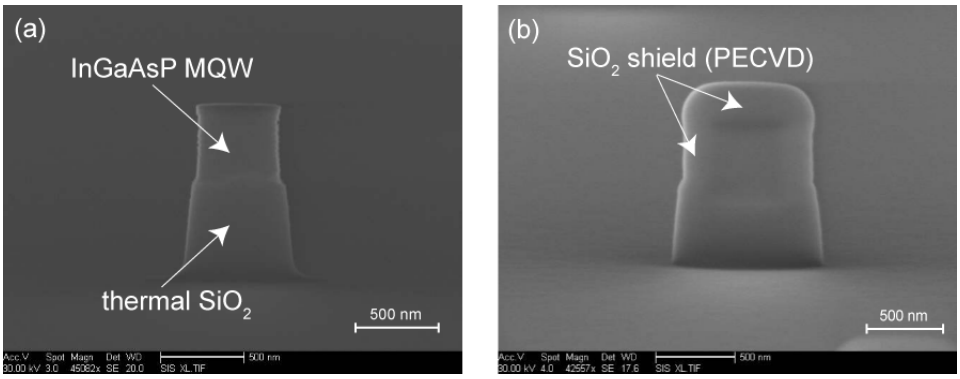

Fig. 18. SEM pictures of: a) a laser pillar after two step RIE b) the same pillar after PECVD of 200nm thick SiO2 layer.

4. 3. Measurements of Wafer Bonded Silicon-III-V Sub-Wavelength Metallo-Dielectric Laser

We use standard micro-photoluminescence setup for optical characterization of the wafer bonded nanolasers. Samples are excited by pumping them through a x20 microscope objective with a 1064nm pulsed fiber laser which has a repetition rate of 300kHz and 12ns pulse width. The light

emitted by a nanolaser is collected with the same objective and passed to the detection system. Using a double 4-f imaging system in conjunction with a pump filter (Semrock RazorEdge long wavelength pass), the samples are imaged onto either an IR InGaAs camera (Indigo Alpha NIR), an electrically cooled InGaAs detector or a monochromator (Spectral Products DK480) with a resolution of 0.35nm, equipped with a cooled InGaAs detector in a lock-in detection configuration. Total power measurements for the light-light curves are performed using a single InGaAs detector. The monochromator is utilized for high resolution measurements in lasing mode to obtain the stimulated emission peak linewidth. Optical measurements at 77K are performed, using Janis ST-500 cryogenic chamber.

We observed room temperature lasing from a sample with approximate gain core radius Rg~450nm and peak wavelength of 1496nm. A kink in the linear scale light-light curve (Figure 19) indicates the onset of lasing at the external threshold pump intensity of 1100W/mm2. The same data set is shown in a log-log plot in the inset graph. For an ideal laser the S-shaped curve represents the transition from photoluminescence (PL) mode (the lower linear section with slope 1) through amplified spontaneous emission (ASE) mode (linear section with a slope steeper than 1) into stimulated emission mode (also slope 1). The unity slope describes a linear dependence of output power to input pump power.

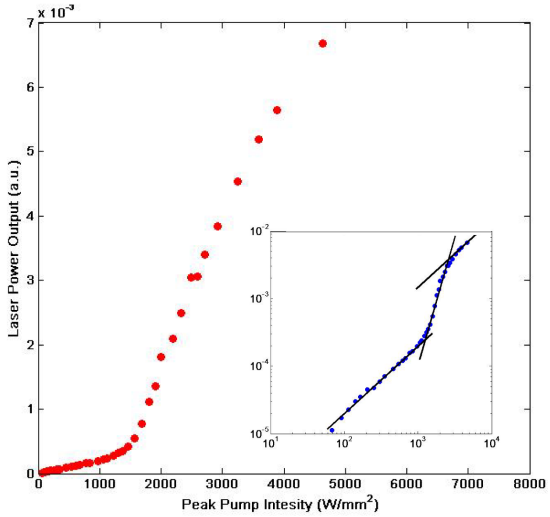

Fig. 19. Room temperature light-light curve for a nanolaser with gain core radius of Rg=450nm. The same data set is shown in the inset as a log-log plot.

Room temperature lasing from smaller samples (Rg ≈250nm) exhibited severe drop of the stimulated emission peak intensity over time, especially after the samples had been subjected

to high pump powers. That prevented reliable light-light curve measurements of small (sub-wavelength) samples. We speculate that high pump powers cause damage to the gain core. To achieve lasing at lower pumping levels, we also performed optical measurements at 77K, with samples placed in a cryogenic chamber. The light-light curves for both Rg ≈450nm (Figure 20) and 250nm (Figure 21) are presented, with the corresponding log-log curves on the inset graphs.

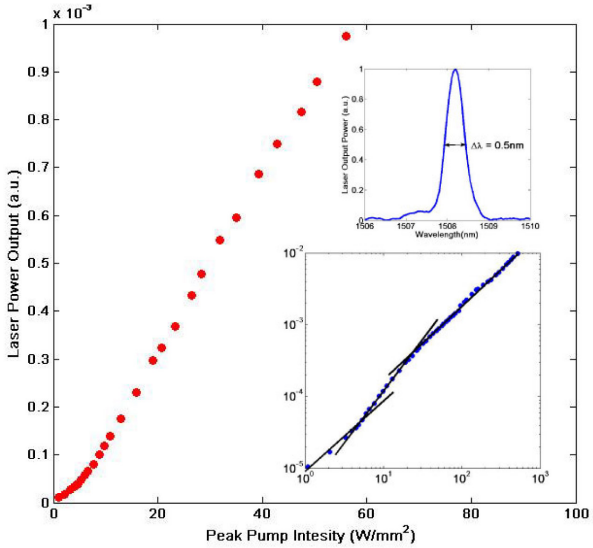

Fig. 20. The light-light curve for a nanolaser with gain core radius of Rg≈450nm at 77K. The same data set is shown in the bottom inset graph as a log-log plot. The upper inset is the lasing spectrum taken with monochrometer; measured linewidth is 0.5nm

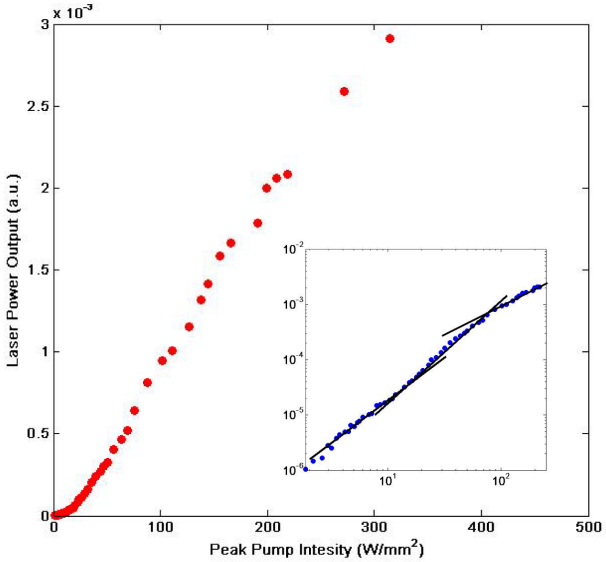

Fig. 21. Light-light curve for a laser with Rg ≈250nm at 77K with the corresponding log-log plot in the inset graph.

For the nanolaser with Rg~450nm and peak wavelength of 1508nm, the threshold at 77K is reduced to 100W/mm2, which is approximately 10 times lower compared to the RT results for

a sample of the same geometry. The linewidth is measured to be 0.5nm, from the high-resolution spectrum shown on the upper inset of Figure 20. The smooth ASE transition region and reduced threshold pump density of the S-curve at 77K are determined by increased material gain, suppressed spectral broadening, enhanced cavity Q and much lower non-radiative recombination rates at cryogenic temperatures [48, 49].

For the 250nm sample the lasing wavelength is 1527nm and the threshold is about 12W/mm2, as shown in Figure 21. The slope of the PL-related linear part of the log-log curve (inset of Figure 21) is around 1.2, in contrast to the samples with Rg ≈450nm, for which the slope is close to unity. The PL region slope larger than unity indicates that significant fraction of recombination events is by single-particle non-radiative processes, such as surface recombination [50]. In the smaller nanolasers, surface recombination is likely to be responsible for the high PL slope, since the ratio of the gain core surface area to it's volume for the sample with Rcore=250nm is much greater compared to one for the sample with Rcore=450nm and thereby, must introduce many more non-radiative recombination centers. Along with the problem of dramatic drop in stimulated emission intensity under optical pumping, this is an interesting issue to be further investigated.

In summary, we demonstrated a wafer bonded subwavelength scale laser that can be integrated onto a silicon platform. We observe room temperature lasing from near-subwavelength structures with gain core radius Rg ≈450nm and cryogenic temperature operation for sub-wavelength structures with Rg of 250nm. The results for the optically pumped lasers are expected to improve through further optimization of the fabrication process. We believe that our approach to realization of sub-wavelength scale coherent sources, combined with the latest III-V-to-Si wafer bonding solutions, is a promising path for the realization of highly integrated and miniaturized room temperature silicon photonic devices. In addition, our unique metal-dielectric resonator design is of interest for a number of applications, such as on-chip communication, optical interconnects, sensing and storage.

5. 0. Thresholdless Nanoscale Coaxial Lasers

Development of manufacturable technology for compact, ultrasmall volume, highly efficient and ultrafast sources of coherent radiation that operate without gain threshold will enable efficient

conversion of information from electrical to optical domain at Terahertz frequencies (i.e., above 300 GHz). Such new sources will open up a new paradigm in design and manufacturing nanoscale systems that will revolutionize numerous applications, including: ultralow energy communication and switching for future computing platforms; ultrafast switching for future computing; and biomedical and chemical sensors with ultrahigh sensitivity and specificity. A schematic comparison of conventional and a thresholdless laser (see Fig. 22) clearly show that for low-energy on-chip interconnection applications, the conventional lasers will need to be replaces by thresholdless nanolasers.

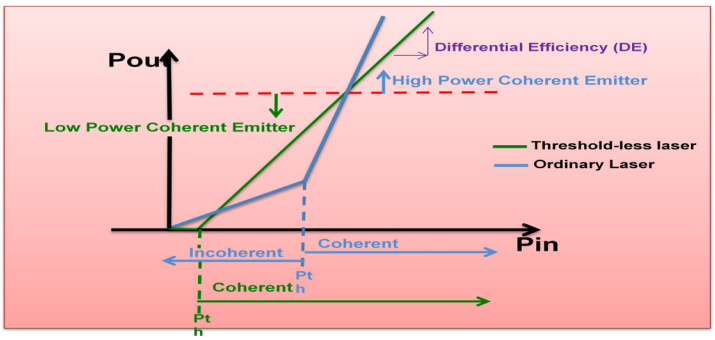

Fig. 22. Schematic comparison showing emitted power vs the pump power for a conventional and a threshold less lasers.

In the emerging field of nano-scale laser sources, with a high spontaneous emission β factor and pronounced Purcell effect (enhancement or inhibition of spontaneous emission into the lasing mode compared to emission into free space, characterized by Purcell factor), the kink in the log-scale light-light curve gets smoothed out and becomes less recognizable. Thresholdless laser behavior would imply a smooth curve throughout the entire pumping region, until saturation is reached. Much attention has been paid on better differentiating the various regions of the light-light curve at low pump powers, which would serve as a useful tool to characterize coherent emission of multimode large scale lasers. Consequently, accurate model of sub-threshold behavior, which is not of crucial importance for large-scale lasers, has not been investigated and understood for single mode nanoscale emitters.

The cavity quantum electrodynamic (QED) effects caused by the interaction of the matter and electromagnetic field in sub-wavelength structures have been the subject of intense research in recent years [51]. The generation of coherent radiation in nanostructures has attracted considerable interest, owing both to the QED effects that emerge in small volumes, and the

potential of these devices for future applications, ranging from on-chip optical communication to ultrahigh resolution and high throughput imaging/sensing/spectroscopy. Research efforts are directed at developingthe "ultimate nanolaser": a scalable, low threshold, efficient source of radiation that operates at room-temperature, and occupies a small volume on a chip [52]. Different have been proposed for the realization of this ultimate nanolaser, namely micro-disk [1], photonic bandgap [11], and more recently metallic [8, 53], metallo-dielectric [24, 30, 40, 54], and plasmonic [55, 41] resonators. However, so far progress toward the ultimate nanolaser has been hindered by the lack of a systematic approach to scale down the size of the laser cavity without significantly increasing the threshold power required for lasing. Here we present a new family of nano-cavities, coaxial nanostructure that solve the resonator scalability challenge due to its unique geometry and metal composition. Using these new nano-cavities, we demonstrate the smallest room temperature, continuous-wave, telecom laser to date. More importantly, for the first time, we demonstrate thresholdless lasing with a broadband gain medium. Besides their applications in the realization of deep sub-wavelength lasers, the nanoscale coaxial resonators are the first step toward unveiling the potential of QED objects and meta-materials in which atom-field interactions generate new functionalities [56, 57].

5. 1. Design and Fabrication of Thresholdless Nanoscale Coaxial Lasers

The miniaturization of laser resonators using dielectric or metallic material structures, faces two challenges: (i) the (eigen-) mode scalability, implying the existence of self-sustained electromagnetic field regardless of the cavity size, and (ii) the unbalanced rate of decrease in optical gain vs. cavity loss which results in large and/or unattainable lasing threshold as the volume of the resonator is reduced [20]. In this section, we describe and demonstrate a new approach to nano-cavity design that resolves both challenges: Firstly, sub-wavelength size nano-cavities with modes far smaller than the operating wavelength are realized by designing a plasmonic coaxial resonator that supports the cutoff-free transverse electromagnetic (TEM) mode. Secondly, the high lasing threshold for small resonators is reduced by utilizing cavity QED effects, causing high coupling of spontaneous emission into the lasing mode.[16,17] When fully exploited, this approach can completely eliminate threshold constraint by reaching so-called *thresholdless* lasing, which occurs when every photon emitted by the gain medium is funneled into the lasing mode 58, 59].

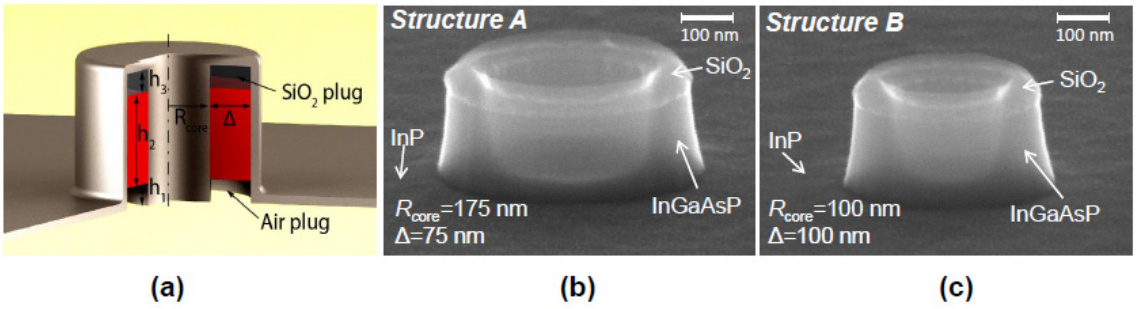

Fig. 23. Nanoscale coaxial laser cavity. (a) Schematic of a coaxial laser cavity. (b) and (c) SEM micrographs of the constituent rings in *Structure A* and *Structure B*, respectively. The side view of the rings comprising the coaxial structures is seen. The rings consist of SiO_2 on top, and quantum wells gain region underneath.

The coaxial laser cavity is portrayed in Figure 23a. At the heart of the cavity lies a coaxial waveguide that supports plasmonic modes and is composed of a metallic rod enclosed by a metal coated semiconductor ring [60, 61]. The impedance mismatch between a freestanding coaxial waveguide and free space creates a resonator. However, our design uses an additional metal coverage on top of the device and thin, low-index dielectric plugs of silicon dioxide at the top end and air at the bottom end of the coaxial waveguide to improve the mode confinement. The role of the top SiO_2 plug is to prevent the formation of undesirable plasmonic modes at the top metal-gain interface. The lower, air plug is used to allow to couple pump into the cavity and also couple out the light generated in the coaxial resonator. The metal in the sidewalls of the coaxial cavity is placed in direct contact with the semiconductor to ensure the support of plasmonic modes, providing a large overlap between the modes of the resonator and the emitters distributed in the volume of the gain medium. In addition, the metallic coating serves as a heat sink that facilitates room temperature and CW operation.

To reduce the lasing threshold, the coaxial structures are designed to maximize the benefits from the modification of the spontaneous emission due to the cavity QED effects [58, 59]. Because of their small size, the modal content of the nanoscale coaxial cavities is sparse, which is a key requirement to obtain high spontaneous emission coupling into the lasing mode of the resonator. Their modal content can be further modified by tailoring the geometry, i.e. the radius of the core, the width of the ring, and the height of the gain and low index plugs. Note that the number of modes supported by the resonator which can participate in the lasing process is ultimately limited to those that occur at frequencies that coincide with the gain bandwidth of the semiconductor gain material. In this work we use a semiconductor gain medium composed of six

quantum wells of $In_{x=0.56}Ga_{1-x}As_{y=0.938}P_{1-y}$ (10 nm thick)/ $In_{x=0.734}Ga_{1-x}As_{y=0.57}P_{1-y}$ (20 nm thick), resulting in a gain bandwidth that spans frequencies corresponding to the wavelengths in vacuum from 1.26 μm to 1.59 μm at room temperature, and from 1.27 μm to 1.53 μm at 4.5 K [62].

We consider two different geometries shown in Figure 23a, the first, referred to as *Structure A*, has an inner core radius of R_{core}=175 nm, gain medium ring with the thickness of Δ=75 nm, lower plug height of h_1= 20 nm, quantum wells height of 200 nm covered by 10 nm overlayer of InP, resulting in the total gain height of h_2=210 nm, and upper plug height of h_3=30 nm. The second, *Structure B* is smaller in diameter, having R_{core}=100 nm, and Δ=100 nm. The heights of the plugs and gain medium are identical to those of *Structure A*. Figure 23b and 23c show the SEM micrographs of the constituent rings in *Structure A* and *Structure B*, respectively. The two structures are fabricated using standard nanofabrication techniques.

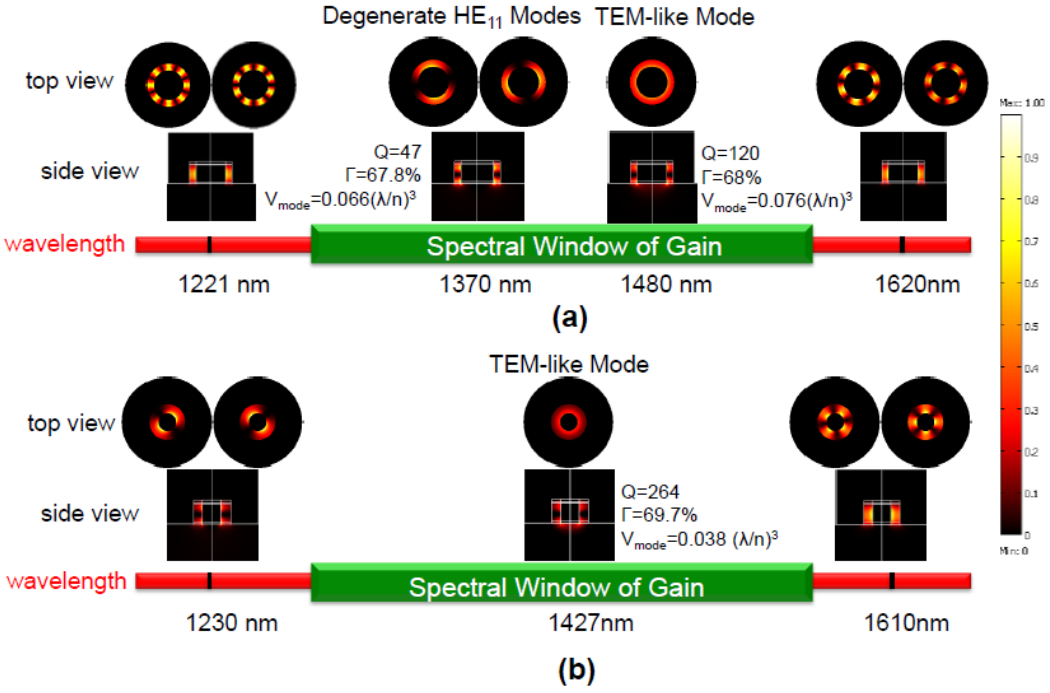

Fig. 24. Electromagnetic simulation of nanoscale coaxial cavities. (a) The modal spectrum of the cavity of *Structure A* at a temperature of 4.5 K. This cavity supports a pair of HE_{11} degenerate modes and the fundamental TEM-like mode in the gain bandwidth. (b) The modal spectrum of the cavity of *Structure B*. This cavity only supports the fundamental TEM-like mode in the gain bandwidth of the quantum wells. In the figures, Q is the quality factor of the mode, Γ is the energy confinement factor to the semiconductor region,[21] and V_{mode} is the effective modal volume.[22] The color bar shows normalized $|E|^2$. Nominal permittivity values are used in this simulation.

Figure 24 shows the modal content of the two structures at 4.5 K, modeled using the 3D Finite Element Method (FEM) eigenfrequency solver in the RF package of COMSOL Multiphysics. Figure 24a shows that for *Structure A* the fundamental TEM-like mode and the

two degenerate HE_{11} modes are supported by the resonator and fall within the gain bandwidth of the gain material. This simulation is also repeated for *Structure A* with room temperature material parameters, showing that for *Structure A* at room temperature, the two degenerate HE_{11} modes are red shifted to 1400 nm, and exhibit a reduced quality factor of $Q \approx 35$, compared to $Q \approx 47$ at 4.5 K. The TEM-like mode is red shifted to 1520 nm with $Q \approx 53$, compared to $Q \approx 120$ at 4.5 K.

Structure B, shown in Figure 24b, supports only the fundamental TEM-like mode at a temperature of 4.5 K. The quality factor $Q \approx 265$ for this mode is higher than that of *Structure A*. In general, the metal coating and the small aperture of the nanoscale coaxial cavity inhibit the gain emitters from coupling into the continuum of the free-space radiation modes [63]. Hence, the single mode cavity of *Structure B* exhibits very high spontaneous emission coupling factor ($\beta \approx 0.99$), approaching the condition for an ideal thresholdless laser [58, 59]. The spontaneous emission factor is calculated by placing randomly oriented and randomly positioned dipoles in the active area of the cavity, and then computing their emitted power at different wavelengths. The β-factor is given by the emitted power that spectrally coincides with the lasing mode, divided by the total emitted power [64].

5. 2. Characterization and Discussion of Thresholdless Nanoscale Coaxial Lasers

Characterization of the nanoscale coaxial lasers was performed under optical pumping with a $\lambda = 1064$ nm laser pump beam in continuous wave and pulsed regime. Excitation of the cavity modes is confirmed by measurements of the far-field emission from the devices.

Figure 25 shows the emission characteristics of the nanoscale coaxial laser of *Structure A* operating at 4.5 K (light-light curve in frame (a), and spectral evolution in frame (b), linewidth in frame (c)), and at room temperature (light-light curve in frame (d), and spectral evolution in frame (e), linewidth in frame (f)). The light-light curves of Figure 25a and 25d show standard laser action behavior, where spontaneous emission dominates at lower pump powers (referred to as the photoluminescence (PL) region), and stimulated emission is dominant at higher pump powers (referred to as the Lasing region). The PL and Lasing region are connected through a pronounced transient region, referred to as amplified spontaneous emission (ASE). The evolution of the spectrum shown in Figures 25b and 25e also confirms the three regimes of operation, PL,

ASE, and Lasing. The spectral profiles at low pump powers reflect the modification of spontaneous emission spectrum by the cavity resonances depicted in Figure 24a. The linewidth of the lasers shown in Figures 25cand 25f narrows with the inverse of the output power at lower pump levels (the solid trend line). This is in agreement with the well-known Schawlow-Townes formula for lasers operating below threshold [65]. Around threshold, the rapid increase of the gain-index coupling in semiconductor lasers slows down the narrowing of the linewidth, until carrier pinning resumes the modified Schawlow-Townes inverse power narrowing rate [66, 67]. In practice, only a few semiconductor lasers are shown to have above-threshold linewidth behavior that follows the modified Schawlow-Townes formula. In most reported lasers, the linewidth behavior distinctly differs from the inverse power narrowing rate. The mechanisms affecting the above-threshold linewidth, especially for lasers with high spontaneous emission coupling to the lasing mode, are still a subject of research [68-70].

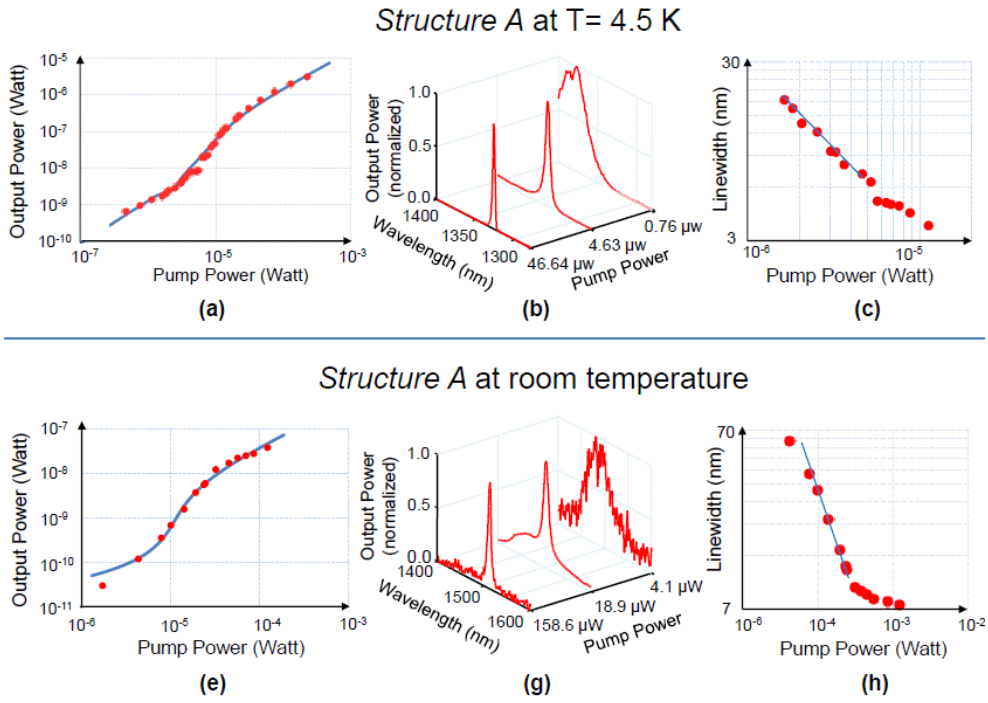

Fig. 25. Optical characterization of nanoscale coaxial cavities, light-light curve, linewidth vs. pump power, and spectral evolution diagram for lasers with threshold. Lasing in *Structure A*. (a) Light-light curve, (b) Spectral evolution and (c) Linewidth evolution at 4.5 K, (d) Light-light curve, (e) Spectral evolution and (f) Linewidth at room temperature. The pump power is calculated as the fraction of the power incident on the laser aperture. The solid curves in (a) and (d) are the best fit of the rate equation model. The resolution of the monochromator was set to 3.3 nm.

A rate-equation model is adopted to study the dynamics of the photon-carriers interaction in the laser cavities. The light-light curves obtained from the rate equation model for the laser of *Structure A* are shown as solid blue lines in Figures 25a and 25d. For the laser operating at 4.5 K, by fitting the rate equation model to the experimental data, we found that almost 20 percent of the spontaneous emission is coupled to the lasing mode, which is assumed to be the mode with the highest quality factor (TEM-like mode). This assumption is validated by examining the far-field radiation pattern and the polarization state of the output beam. At room temperature, the surface and Auger non-radiative recombination processes dominate. As the carriers are lost through non-radiative channels, the ASE kink of the laser is more pronounced, and, as expected, the laser threshold shifts to higher pump powers.

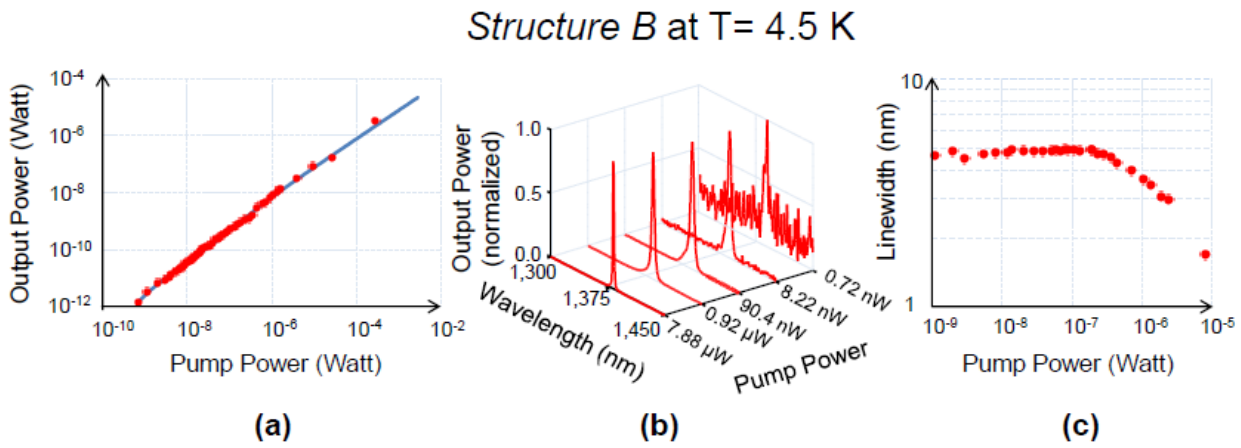

Fig. 26. Optical characterization of nanoscale coaxial cavities, light-light curve, linewidth vs. pump power, and spectral evolution diagram for thresholdless lasers. Thresholdless lasing in *Structure B*. (a) Light-light curve, (b) Spectral evolution, and (c) Linewidth evolution at 4.5 K. The pump power is calculated as the fraction of the power incident on the laser aperture. The solid curve in (a) is the best fit of the rate equation model. The resolution of the monochromator was set to 1.6 nm.

Next, we examine the emission characteristics of *Structure B*. According to the electromagnetic analysis (Figure 24b), this structure is expected to operate as a thresholdless laser, as only one non-degenerate mode resides within the gain medium's emission bandwidth. The emission characteristics of *Structure B* at 4.5 K are shown in Figure 26. The light-light curve of Figure 26a, that follows a straight line with no pronounced kink, agrees with the thresholdless lasing hypothesis. The thresholdless behavior is further manifested in the spectral evolution, seen in Figure 26b, where a single narrow, Lorentzian-like emission is obtained over the entire five-orders-of-magnitude range of pump power. This range spans from the first signal detected above the detection system noise floor at 720 pW pump power, to the highest pump power of more than

100 μW. Since the homogenously broadened linewidth of the gain medium is larger than the linewidth of the observed emission, the emission profile is attributed to the cavity mode. The measured linewidth at low pump power ($\Delta\lambda_{FWHM}\approx5$ nm) that agrees with the transparency cavity Q-factor of the TEM-like mode, as well as the radiation pattern, confirms the electromagnetic simulation given in Figure 24b. The proof that the device indeed reaches lasing is further substantiated by the careful study of the linewidth behavior. At low pump levels, the linewidth depicted in Figure 26c is almost constant, and does not narrow with output power, implying that the linewidth shows no subthreshold behavior [65,67]. The lack of variation of linewidth with pump power is most likely the result of the increasing gain-index coupling, that is a well-known around-threshold behavior in semiconductor lasers [66, 67].Another indication, and more decisive proof, that *Structure B* does not exhibit sub-threshold behavior is that the linewidth narrowing above the 100 nW pump power level does not follow the inverse power narrowing rate that is clearly identified in *Structure A*. This narrowing corresponds to the carrier-pinning effect, as further corroborated by the results of the rate-equations model for the carrier density. To the best of our knowledge, this linewidth behavior, though predicted in theory [68-70], has never been reported in any laser, and is unique to our thresholdless laser. The light-light curve obtained from the rate equation model for the laser of *Structure B* at 4.5 K is shown by the solid blue line in Figure 26a. Best fit of our rate equation model to the experimental data is achieved if 95 percent of the spontaneous emission is coupled to the lasing mode ($\beta=0.95$). The deviation from the $\beta=0.99$ predicted by the electromagnetic simulation can be attributed to other non-radiative recombination processes that have not been considered in the rate equation model, and to the spectral shift of the mode at higher pump levels that causes variations in the available gain for the mode. In summary, all the experimental observations, including output spectrum and beam profile, electromagnetic simulations, rate equation model, and comparison with the non-thresholdless lasers, suggest thresholdless lasing as the only plausible hypothesis that satisfactorily explains all aspects of the emission of the light emitting device, based on *Structure B* at 4.5 K.

The thresholdless lasing in nanoscale coaxial cavities clearly differs from the state-of-the-art, high quality factor, photonic bandgap structures [71]. In the latter, near-thresholdless lasing is achieved in a quantum dot gain medium system with spectrally narrow band emission, and relies extensively on tuning of the cavity mode to the center of the quantum dot emission

spectrum [71]. In the former, thresholdless lasing in a broadband gain medium is achieved with a low quality factor, single-mode metal cavity. Smaller size, straightforward fabrication procedure, and better thermal properties are just a few of the advantages of nanoscale coaxial cavities for the realization of thresholdless lasing.

In summary, with nanoscale coaxial structures, we have successfully demonstrated room temperature, continuous-wave lasing, as well as low temperature thresholdless lasing in a spectrally broadband semiconductor gain medium. Owing to the fundamental TEM-like mode with no cutoff, these cavities show ultra-small mode confinement, offer large mode-emitter overlap that results in optimal utilization of the pump power, and provide multifold scalability. Further developments toward electrical pumping of thresholdless nanoscale coaxial lasers that can operate at room temperature are in progress. The implication of our work is threefold. Firstly, the demonstrated nanoscale coaxial lasers have a great potential for future nano-photonic circuits on a chip. Secondly, thresholdless operation and scalability provide the first systematic approach toward the realization of QED objects and functionalities, specifically the realization of quantum meta-materials. Finally, this new family of resonators paves the way to in-depth study of the unexplored physics of emitter-field interaction,

6. 0. Future Research Directions Lasers

Although the NACHOS program has concluded on March 31, 2013, the research team is continuing its work on metallo-dielectric and thresholdless nanolasers. Current research directions include electrically pumped coaxial geometry devices, integration of nanolasers with silicon-on-insulator chip-scale waveguides, and gain material grown radially around a nanowire core. Theoretical analysis of nanolaser rate equations and linewidth behavior is also ongoing.

6. 0 References

1. McCall, S. L., Levi, A. F. J., Slusher, R. E., Pearton, S. J. & Logan, R. A. Whispering-gallery mode microdisk lasers. Appl. Phys. Lett. 60, 289–291 (1992).

2. Jin Shan, P., Po Hsiu, C., Tsin Dong, L., Yinchieh, L. & Kuochou, T. 0.66 mm InGaP/InGaAlP single quantum well microdisk lasers. Jpn J. Appl. Phys., Part 2
37, L643–L645 (1998).

3. Md Zain, A. R., Johnson, N. P., Sorel, M. & De La Rue, R. M. High quality-factor 1-D-suspended photonic crystal/photonic wire silicon waveguide microcavities.
IEEE Photon. Technol. Lett. 21, 1789–1791 (2009).

4. Akahane, Y., Asano, T., Song, B. S. & Noda, S. High-Q photonic nanocavity in a two-dimensional photonic crystal. Nature 425, 944–947 (2003).

5. Song, Q., Cao, H., Ho, S. T. & Solomon, G. S. Near-IR subwavelength microdisk lasers. Appl. Phys. Lett. 94, 061109 (2009).

6. Smotrova, E. I., Nosich, A. I., Benson, T. M. & Sewell, P. Optical coupling of whispering-gallery modes of two identical microdisks and its effect on photonic molecule lasing. IEEE J. Sel. Top. Quantum Electron. 12, 78–85 (2006).

7. Min, B. K. et al. High-Q surface-plasmon–polariton whispering-gallery microcavity. Nature 457, 455–458 (2009).

8. Hill, M. T. et al. Lasing in metallic-coated nanocavities. Nature Photon. 1, 589–594 (2007).

9. Johnson, P. B. & Christy, R. W. Optical constants of the noble metals. Phys. Rev. B 6, 4370–4379 (1972).

10. Hill, M. T. et al. Lasing in metal–insulator–metal sub-wavelength plasmonic waveguides. Opt. Express 17, 11107–11112 (2009).

11. O. Painter, R. K. Lee, A. Scherer, A. Yariv, J. D. O'Brien, P. D. Dapkus, and I. Kim, Science **284**, 1819 (1999).

12. C.-K. Lin, D. P. Bour, J. Zhu, W. H. Perez, M. H. Leary, A. Tandon, S. W. Corzine, and M. R. T. Tan, IEEE J. Sel. Top. Quantum Electron. **9**, 1415 (2003).

13. A. V. Maslov and C. Z. Ning, Proc. SPIE **6468**, 64680I (2007).

14. V. Krishnamurthy and B. Klein, IEEE J. Quantum Electron. **44**, 67 (2008).

15. Nezhad, M. P., Tetz, K. & Fainman, Y. Gain assisted propagation of surface plasmon polaritons on planar metallic waveguides. Opt. Express 12, 4072–4079 (2004).

16. P. Yeh, A. Yariv, and E. Marom, J. Opt. Soc. Am. **68**, 1196 (1978).

17. A. Mizrahi and L. Schächter, Opt. Express **12**, 3156 (2004).

18. M. Miyagi, A. Hongo, and S. Kawakami, IEEE J. Quantum Electron. **19**, 136 (1983).

19. A. E. I. Smotrova and A. I. Nosich, Opt. Quantum Electron. **36**, 213 (2004).

20. E. D. Palik, *Handbook of Optical Constants of Solids* (Academic, 1985).21. L. Novotny and C. Hafner, Phys. Rev. E **50**, 4094 (1994).

22. Goebel, E. O., Luz, G. & Schlosser, E. Optical gain spectra of InGaAsP–InP double heterostructures. IEEE J. Quantum Electron. 15, 697–700 (1979).

23. Korbl, M., Groning, A., Schweizer, H. & Gentner, J. L. Gain spectra of coupled InGaAsP/InP quantum wells measured with a segmented contact traveling wave device. J. Appl. Phys. 92, 2942–2944 (2002).

24. Mizrahi, A. et al. Low threshold gain metal coated laser nanoresonators. Opt. Lett. 33, 1261–1263 (2008).

25. Chua, C. L., Thornton, R. L., Treat, D. W. & Donaldson, R. M. Independently addressable VCSEL arrays on 3 mm pitch. IEEE Photon. Technol. Lett. 10, 917–919 (1998).

26. Altug, H., Englund, D. & Vuckovic, J. Ultrafast photonic crystal nanocavity laser. Nature Phys. 2, 484–488 (2006).

27. Rao, Z. L., Hesselink, L. & Harris, J. S. High-intensity bowtie-shaped nanoaperture vertical-cavity surface-emitting laser for near-field optics. Opt. Lett. 32, 1995–1997 (2007).

28. D. A. Miller, "Optical Interconnects to Silicon," IEEE J. Select. Topics Quantum Electron., **6**, 1312-1317 (2000).

29. E. Purcell, "Spontaneous emission probabilities at radio frequencies," Phys. Rev., 69, 681 (1946).

30. M. P. Nezhad, A. Simic, O. Bondarenko, B. Slutsky, A. Mizrahi, L. Feng, V. Lomakin, and Y. Fainman, "Room-temperature subwavelength metallo-dielectric lasers," Nat. Photonics 4, 395-399 (2010).

31. T. Baba, "Photonic Crystals and Microdisk Cavities Based on GaInAsP-InP System," IEEE J. Sel. Top. Quantum Electron., 3, 808-830 (1997) .

32. T. Baba, M. Fujita, A. Sakai, M. Kihara, and R. Watanabe, "Lasing Characteristics of GaInAsP-InP Strained Quantum-Well Microdisk Injection Lasers with Diameter of 2-10 μm," IEEE Photon. Tech. Lett., 9, 878-880 (1997) .

33. M. Asada, and Y. Suematsu, "Density-Matrix Theory of Semiconductor Lasers with Relaxation Broadening Model-Gain and Gain-Suppresion in Semiconductor Lasers," IEEE J. Quantum Electron., **21**, 434-442 (1985) .

34. Z. Liu, J. M. Shainline, G. E. Fernandes, J. Xu, J. Chen, and C. F. Gmachl, "Continuous-wave subwavelength microdisk lasers at $\lambda = 1.53$ μm," Opt. Express **18**, 19242-19248 (2010).

35 J. Van Campenhout, P. Rojo-Romeo, D. Van Thourhout, C. Seassal, P. Regreny, L. D. Cioccio, J.-M. Fedeli, and R. Baets, "Thermal Characterization of Electrically Injected Thin-Film InGaAsP Microdisk Lasers on Si," J. Lightw. Technol., **25**, 1543-1548 (2007) .

36. F. Albert, T. Braun. T. Heindel, C. Schnedier, S. Reitzenstein, S. Höfling, L. Worschech, and A. Forchel, "Whispering gallery mode lasing in electrically driven quantum dot micropillars," Appl. Phys. Lett., 97, 101108 (2010).

37. H. Rong, R. Jones, A. Liu, O. Cohen, D. Hak, A. Fang and M. Paniccia, "A continuous-wave Raman silicon laser," Nature, vol. 433, pp. 725-728, Feb. 17, 2005.

38 L. Dal Negro, "Light emission from silicon nanostructures: Past, present and future perspectives," in http://ieeexplore.ieee.org/xpls/abs_all.jsp?arnumber=5224856&tag=1, 2009,

39. A. W. Fang, H. Park, O. Cohen, R. Jones, M. J. Paniccia and J. E. Bowers, "Electrically pumped hybrid AlGaInAs-silicon evanescent laser " Optics Express, vol. 14, no 20, pp. 9203, 2006

40. K. Yu, A. Lakhani, and M. C. Wu, "Subwavelength metal-optic semiconductor nanopatch lasers," Opt. Express 18, 8790- 8799 (2010).

41. R. F. Oulton, V. J. Sorger, T. Zentgraf, R. -M. Ma, C. Gladden, L. Dai, G. Bartal, and X. Zhang, "Plasmon lasers at deep subwavelength scale," Nature 461, 629-632 (2009).

42. H. -G. Park, S. -H. Kim, S. -H. Kwon, Y. -G. Ju, J. -K. Yang, J. -H. Baek, S. -B. Kim, and Y. -H. Lee, "Electrically Driven Single-Cell Photonic Crystal Laser," Science 305, 1444-1447 (2004).

43. R. Ma, R. F. Oulton, V. J. Sorger, G. Bartal and X. Zhang. (2011, 12-19). Room-temperature sub-diffraction-limited plasmon laser by total internal reflection. Nature Materials 10(2), pp.

110-113, Feb. 2011. DOI: 10.1038/nmat2919 Available: http://www.nature.com/nmat/current_issue/.

44. F. Niklaus, G. Stemme, J. -. Lu and R. J. Gutmann, "Adhesive wafer bonding," J. Appl. Phys., vol. 99, issue 3, pp. 031101, 2006. DOI: 10.1063/1.2168512

45. D. Liang, J. E. Bowers, D. C. Oakley, A. Napoleone, D. C. Chapman, L. -. Chen, P. W. Juodawlkis and O. Raday, "High-Quality 150 mm InP-to-Silicon Epitaxial Transfer for Silicon Photonic Integrated Circuits," ECS, vol. 12, pp. H101, 2009.

46. D. Liang, A. W. Fang, H. Park, T. E. Reynolds, K. Warner, D. C. Oakley and J. E. Bowers, "Low-Temperature, Strong SiO2-SiO2 Covalent Wafer Bonding for III–V Compound Semiconductors-to-Silicon Photonic Integrated Circuits," J Electron Mater, vol. 37, pp. 1552 <last_page> 1559, 2008.

47. D. Pasquariello and K. Hjort, "Plasma-assisted InP-to-Si low temperature wafer bonding," Selected Topics in Quantum Electronics, IEEE Journal of, vol. 8, pp. 118-131, 2002.

48. T. Baba and D. Sano. (2003, Low-threshold lasing and purcell effect in microdisk lasers at room temperature. IEEE J. Sel. Top. Quantum Electron. 9(5), pp. 1340.

49. L. A. Coldren and S. W. Corzine, Diode Lasers and Photonic Integration Circuits. Wiley-Interscience, New York 1995.

50. K. Srinivasan, M. Borselli, O. Painter, A. Stintz and S. Krishna, "Cavity Q, mode volume, and lasing threshold in small diameter AlGaAs microdisks with embedded quantum dots" Opt. Express, vol. 14, pp. 1094, 2006.

51. Berman, P. (ed.), Cavity Quantum Electrodynamics (Academic, San Diego, 1994).

52. 2. Noda, S., Seeking the ultimate nanolaser. Science 314 (5797), 260–261 (2006)

53. 6. Walther C., Scalari G., Amanti M. I., Beck M., & Faist J., Microcavity laser oscillating in a circuit-based resonator. Science 327 (5972), 1495 (2010)

54. Ding Q., Mizrahi A., Fainman Y., & Lomakin. V., Dielectric shielded nanoscale patch laser resonators. Opt. Lett. 36, 1812–1814 (2011)

55. M. A. Noginov, G. Zhu, A. M. Belgrave, R. Bakker, V. M. Shalaev, E. E. Narimanov, S. Stout, E. Herz, T. Suteewong, and U. Wiesner, "Demonstration of a spaser-based nanolaser," Nature 460, 1110-1113 (2009).

56. Burgos, S. P., deWaele, R., Polman, A., & Atwater, H. A., A single-layer wide-angle negative-index metamaterial at visible frequencies. Nature Materials 9, 407–412 (2010)

57. Jacob, Z. & Shalaev, V. M., Plasmonics goes quantum. Science 28, 463 (2011).

58. Yokoyama, H., Physics and device applications of optical microcavities. Science 256 (5053), 66–70 (1992)

59. Bjork, G. & Yamamoto, Y., Analysis of semiconductor microcavity lasers using rate equations. IEEE J. Quantum Electronics 27, 2386–2396 (1991)

60. Baida, F. I., Belkhir, A., & Van Labeke, D., Subwavelength metallic coaxial waveguides in the optical range: Role of the plasmonic modes. Phys. Rev. B 74, 205419 (2006)

61. Feigenbaum, E. & Orenstein, M., Ultrasmall volume plasmons, yet with complete retardation effects. Phys Rev Lett. 101 (16) 163902 (2008)

62. Benzaquen, R. et al., Alloy broadening in photoluminescence spectra of GaxIn1−xAsyP1−y lattice matched to InP. J. Appl. Phys. 75, no.5, 2633–2639 (1994)

63. Bayer, M. et al., Inhibition and enhancement of the spontaneous emission of quantum dots in structured microresonators. Phys. Rev. Lett. 86 (14), 3168–3171 (2001)

64. Vuckovic, J., Painter, O., Xu, Y., Yariv, A., Scherer, A., Finite-difference time-domain calculation of the spontaneous emission coupling factor in optical microcavities. IEEE J. Quantum Electron. 35, 1168 (1999)

65. Schawlow, A. L. & Townes, C. H., Infrared and optical masers. Phys. Rev. 112 (6), 1940 (1958)

66. Henry, C., Theory of the linewidth of semiconductor lasers, JQE IEEE 18, 2, 259–264 (1982)

67. Björk, G., Karlsson, A., & Yamamoto Y., On the linewidth of microcavity lasers. Appl. Phys. Lett. 60, 304 (1992)

68. Rice, P. R. & Carmichael, H. J., Photon statistics of a cavity-QED laser: A comment on the laser-phase-transition analogy. Phys. Rev. A 50 (5), 4318–4329 (1994)

69. Pedrotti, L. M., Sokol, M., & Rice, P. R., Linewidth of four-level microcavity lasers. Phys. Rev. A 59, 2295 (1999)

70. Roy-Choudhury, K. & Levi, A. F. J., Quantum fluctuations and saturable absorption in mesoscale lasers. Phys. Rev. A 83, 043827 (2011)

71. Strauf, S. et al., Self-tuned quantum dot gain in photonic crystal lasers. Phys. Rev. Lett. 96 (12), 127404/1–4 (2006)